AD-A160 899 LIDAR MULTIPLE SCATTERING/DEPOLARIZATION IN STRATUS CLOUDS(U) AIR FORCE INST OF TECH WRIGHT-PATTERSON AFB OH R L PETRILLA 1985 AFIT/CI/NR-85-142T 1/1

UNCLASSIFIED F/G 4/2 NL

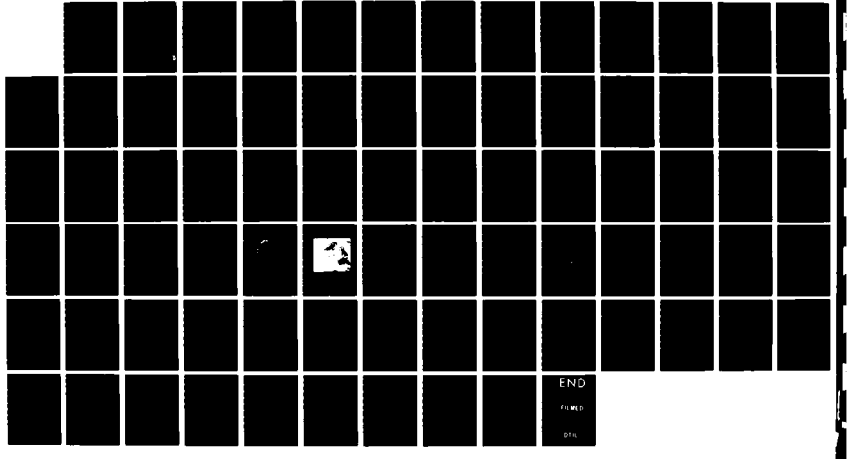

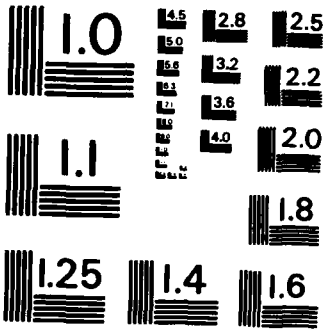

MICROCOPY RESOLUTION TEST CHART
NATIONAL BUREAU OF STANDARDS - 1963 - A

UNCLASS
SECURITY CLASSIFICATION OF THIS PAGE (When Data Entered)

REPORT DOCUMENTATION PAGE

READ INSTRUCTIONS BEFORE COMPLETING FORM

1. REPORT NUMBER: AFIT/CI/NR 85-142T	2. GOVT ACCESSION NO.
3. RECIPIENT'S CATALOG NUMBER	
4. TITLE (and Subtitle): Lidar Multiple Scattering/Depolarization In Stratus Clouds	5. TYPE OF REPORT & PERIOD COVERED: THESIS/DISSERTATION
	6. PERFORMING ORG. REPORT NUMBER
7. AUTHOR(s): Richard Lee Petrilla	8. CONTRACT OR GRANT NUMBER(s)
9. PERFORMING ORGANIZATION NAME AND ADDRESS: AFIT STUDENT AT: The University of Utah	10. PROGRAM ELEMENT, PROJECT, TASK AREA & WORK UNIT NUMBERS
11. CONTROLLING OFFICE NAME AND ADDRESS: AFIT/NR WPAFB OH 45433 - 6583	12. REPORT DATE: 1985
	13. NUMBER OF PAGES: 67
14. MONITORING AGENCY NAME & ADDRESS (if different from Controlling Office)	15. SECURITY CLASS. (of this report): UNCLASS
	15a. DECLASSIFICATION/DOWNGRADING SCHEDULE

16. DISTRIBUTION STATEMENT (of this Report)

APPROVED FOR PUBLIC RELEASE; DISTRIBUTION UNLIMITED

17. DISTRIBUTION STATEMENT (of the abstract entered in Block 20, if different from Report)

18. SUPPLEMENTARY NOTES

APPROVED FOR PUBLIC RELEASE: IAW AFR 190-1

LYNN E. WOLAVER 21 Oct 85
Dean for Research and
Professional Development
AFIT, Wright-Patterson AFB

19. KEY WORDS (Continue on reverse side if necessary and identify by block number)

20. ABSTRACT (Continue on reverse side if necessary and identify by block number)

ATTACHED

DTIC ELECTE NOV 04 1985 S D E

DD FORM 1 JAN 73 1473 EDITION OF 1 NOV 65 IS OBSOLETE

UNCLASS
SECURITY CLASSIFICATION OF THIS PAGE (When Data Entered)

AD-A160 899

DTIC FILE COPY

1 2

LIDAR MULTIPLE SCATTERING/DEPOLARIZATION IN STRATUS CLOUDS

by

Richard Lee Petrilla

Capt, USAF

A thesis submitted to the faculty of

The University of Utah

in partial fulfillment of the requirements for the degree

of

Master of Science

Department of Meteorology

The University of Utah

1985, 67pp

Accession For
NTIS GRA&I
DTIC TAB
Unannounced
Justification
By
Distribution/
Availability Codes
Dist Special
A-1

QUALITY INSPECTED 5

85 11 04 001

LIDAR MULTIPLE SCATTERING INDUCED DEPOLARIZATION IN STRATUS CLOUDS

by

Richard Lee Petrilla

A thesis submitted to the faculty of
The University of Utah
in partial fulfillment of the requirements for the degree of

Master of Science

Department of Meteorology

The University of Utah

December 1985

Copyright © 1985 Richard Lee Petrilla

All Rights Reserved

THE UNIVERSITY OF UTAH GRADUATE SCHOOL

FINAL READING APPROVAL

To the Graduate Council of The University of Utah:

I have read the thesis of Richard Lee Petrilla in its final form and have found that (1) its format, citations, and bibliographic style are consistent and acceptable; (2) its illustrative materials including figures, tables, and charts are in place; and (3) the final manuscript is satisfactory to the Supervisory Committee and is ready for submission to the Graduate School.

31 May 1985
Date

Kenneth Sassen
Member, Supervisory Committee

Approved for the Major Department

J.E. Geisler
Chairman Dean

Approved for the Graduate Council

James L. Clayton
Dean of The Graduate School

84
3-81

THE UNIVERSITY OF UTAH GRADUATE SCHOOL

SUPERVISORY COMMITTEE APPROVAL

of a thesis submitted by

Richard Lee Petrilla

This thesis has been read by each member of the following supervisory committee and by majority vote has been found to be satisfactory.

31 May 1985 — Chairman. Kenneth Sassen

31 May 1985 — K.N. Liou

31 May 1985 — N. Fukuta

ABSTRACT

The contributions of multiple scattering to backscattered depolarization ratios in stratus clouds were investigated using a linearly-polarized ruby lidar system from a site on the southern California coast. The effects of the receiver field of view, lidar elevation angle, and transmitter/receiver beam misalignment on depolarization ratios were investigated.

Results for a 1 mrad transmitter beam width indicate that a receiver field of view of 3 mrad returns an almost threefold increase in backscattered depolarization ratios as opposed to a 1 mrad field of view. The effects caused by changing the elevation angle appear to be related to the cloud microphysical processes occurring above the cloud base. Deliberate beam misalignment produces significant alterations in the lidar returns, demonstrating the importance of maintaining proper alignment.

In the future, the lidar should be used in conjunction with in situ microphysical observations and a program of theoretical studies to assess the degree to which the lidar data can be related to specific stratus cloud properties.

This thesis is dedicated to my wife Diane, for her understanding and fortitude when I wanted to quit.

TABLE OF CONTENTS

LIST OF TABLES

LIST OF FIGURES

ACKNOWLEDGMENTS

I wish to express my appreciation to Dr. Kenneth Sassen, whose assistance and guidance made this thesis possible. I also wish to thank my other committee members, Dr. Kuo-Nan Liou and Dr. Norihiko Fukuta for their aid and encouragement.

I would also like to thank Michael Griffin, Jeff Koenig, and Glenn Ahrens who took time from their busy schedules to assist me when the going was tough.

The research reported in this thesis was supported by the National Science Foundation under Grant ATM-82-10709. The lidar data were originally collected in connection with Contract No. F19628-81-K-0042 from the Department of the Air Force.

CHAPTER 1

INTRODUCTION

1.1 Background

In 1803 an Englishman, Luke Howard, first classified clouds according to type by using their shape, shading, and general appearance. To this day, a need still exists to determine the exact composition and structure of the various clouds he classified back in 1803. Information pertaining to the amount and phase of hydrometeors, and to their type and location, can improve our understanding of cloud structure and precipitation development. These measurements are invaluable in forming more precise climatological and forecasting models of the atmosphere.

Recently, researchers at the University of Utah (Sassen et al., 1985) discovered supercooled liquid water in cirrus clouds, where in the past it was thought that only ice occurred. Discoveries such as this dictate a change in the way the microstructure and microphysical processes occurring inside a cloud are viewed.

Instrumentation for looking at cloud composition has been developed and falls into three broad categories: 1) in situ sampling from airborne platforms (e.g., aircraft, balloons, etc.); 2) in situ sampling from surface stations (e.g., rain gauges, mountain-top observations, etc.); and 3) remote sensing (e.g., radars, radiometers, laser radars, etc.). Each system has unique advantages and

disadvantages. Each specific piece of equipment is different and no single remote sensor can supply all of the information required for atmospheric studies.

In the field of remote sensing, microwave radars are the dominant instruments used. For many years, large wavelength radars have proven very useful for looking at storm structure, and new techniques have been developed for Doppler radars to infer cloud composition from particle fall velocities. However, in many respects radar does not show as great a sensitivity to cloud composition as the laser radar (lidar).

1.2 The Applicability of Lidar

Over the past 10-15 years there has been an increasing use of lidar in cloud physics research. The principle of lidar remote sensing is analogous to radar remote sensing, with energy radiated in the visible spectrum as opposed to energy in the microwave region. Much of the traditional phemonena associated with microwave radars (e.g., the bright band) exist with lidars (Sassen, 1976a).

When a linearly polarized pulse of high intensity light is directed toward a cloud, both the strength and the linear depolarization of the returned signal provide information on the phase, type, and number or size of cloud particles. Even though this ability exists, the amount of lidar research which has been published is not great, perhaps due to a lack of confidence in the interpretation of lidar field data. A part of this lack of confidence arises from the fact that not enough is known about the effects of multiple scattering on lidar returns. Multiple scattering processes have been studied both

theoretically and experimentally in the laboratory and field, and there is a large variance in reported depolarization ratios. It is even uncertain to what extent the laboratory environment can actually mimic the real atmosphere. There is a need to better understand the physical properties of the atmospheric target, and how the scattering properties are affected by the design of the lidar system. The only way to do this is to use the lidar in the atmosphere and compare the results to laboratory and theoretical findings. Recently, a considerable amount of research has been accomplished in the laboratory, and it is logical that the lidar will again be used in the real atmosphere.

1.3 The Stratus Problem

In the past, most efforts in the field of cloud physics concentrated mainly on devising models of the structure and development of convective clouds. Although convective clouds are of great significance, they are observed much less frequently than other cloud types, such as stratus and stratocumulus. During the past 20 to 30 years there has been considerable success in studying the dynamics of stratiform cloud masses. Fundamental laws describing their formation, development, and dissipation have been formulated. Satellite observations have also become increasingly available and sophisticated in the past 10-15 years, providing valuable descriptions of stratus clouds on the synoptic and mesoscales. A better understanding of cloud composition and structure in the microscale is needed to go along with the synoptic approach.

Stratiform clouds are perhaps most important when the radiation

and energy balance of the atmosphere/ocean system are considered. As Randal et al. (1984) pointed out:

> . . . marine stratus and stratocumulus cloud systems are likely to strongly influence the climate and climate change. Their high albedos (30-40%) compared with the ocean background (10%) give rise to large deficits in the absorbed solar radiative flux at the top of the atmosphere, while their low altitude prevents significant compensation in thermal emission. A mere 4% increase in the area of the globe covered by low level stratus clouds would be sufficient to offset the 2-3°K predicted rise in global temperature due to a doubling of CO_2.

The effect of humanity on the environment has been in the forefront of news for many years. It is debatable whether the earth is cooling or warming and what the effects are of acid rain, CO_2 doubling, and deforestation. These are difficult questions and a better understanding of cloud processes is needed to answer them.

In conjunction with a better understanding of cloud processes, a better knowledge of water cloud microphysical properties is needed. Lidar is one of the tools capable of easily and economically probing water clouds. This research was undertaken in order to better understand the multiple scattering process in water clouds and particularly in stratus clouds. The signature of multiple scattering is present in the backscattered depolarization of the laser pulse, and it is clearly necessary to better understand this scattering process in order to improve our knowledge of the structure of stratus clouds when probed with lidar.

CHAPTER 2

LIDAR PRINCIPLES AND SCATTERING THEORY

2.1 The Lidar Equation

As previously mentioned, both the radar and lidar have similar characteristics, including their governing equations. Battan (1973) gave a complete derivation of the monostatic radar equation and Sassen (1976b) gave the equivalent derivation for lidar. The final form of the equation used here is from Sassen (1977a), where P(R) is the power returned to the receiver in the polarization planes both parallel and orthogonal to the transmitter as a function of range R. This equation assumes that the laser beam is filled with targets, that no energy scattered out of the beam is collected by the receiver, and that the transmitter and receiver beam widths are equal and in parallel alignment.

$$P(R)_{\parallel,\perp} = \frac{P_t h A_r}{8\pi R^2} f(R)\ \beta'(R)_{\parallel,\perp} \exp\left[-2R\eta\sigma(R)\right] \quad , \tag{2.1}$$

where P_t is the transmitted (linearly polarized) power (W), h the laser pulse length (m), A_r the effective collecting area of the receiver (m^2), f(R) the lidar cross over function, $\beta'(R)$ the volume backscatter coefficient (km^{-1}), η the multiple scattering correction factor, and $\sigma(R)$ the extinction coefficient (km^{-1}).

2.1.1 System Constants

With reference to the seven terms on the right-hand side of Eq. (2.1), the first three terms in the numerator are commonly referred to as system constants. Although the first two terms may change slightly from laser pulse to pulse and so must be monitored, the third term, the effective collecting area of the receiver, is fixed by the design of the lidar receiver (i.e., the telescope).

2.1.2 The Cross Over Function

The fourth term in Eq. (2.1) is the cross over function, the first of the range-dependent terms. Due to the design constraints of a high-power monostatic lidar system imposed by the size of the laser, it is usually necessary to physically separate the transmitter and receiver on an optical table and align their axes in parallel. Consequently, the transmitter pulse and the receiver field of view do not overlap until they are some distance from the lidar. This distance is proportional to the physical separation between the transmitter and receiver on the optical table, and to the laser beam transmitter and receiver beam width angles. Measurements obtained from targets within the range where there is little or no overlap (generally a few hundred meters or less) must be examined with caution, since the energy returned from such short ranges can only result from multiple scattered radiation, assuming negligible side lobe radiation is present.

However, in these experiments, a variable diaphragm was used so that the receiver field of view could be changed between 1 and 3 mrad.

This capability is a useful adjunct for multiple scattering studies since, in dealing with a dense target, the amount of backscattered power received with a lidar becomes a function of the beam widths used. In effect, this capability changes $f(R)$ and can lead to a violation of the lidar equation, Eq. (2.1), when equal transmitter and receiver beam widths are not used.

2.1.3 Single Scattering Coefficients

Since the first four terms in Eq. (2.1) can be considered to be constants, the returned laser power from atmospheric targets depends on the range and the scattering coefficients, $\beta'(R)$ and $\sigma(R)$. Both scattering coefficients are directly proportional to the cross-sectional areas and the particle concentrations per unit volume. Experimental determinations of the scattering coefficients have been obtained, and typical values are presented in Table 2.1.

One of the major problems associated with lidar remote sensing data interpretation has to do with deriving the values of both $\beta'(R)$ and $\sigma(R)$. For radar, under typical conditions, microwave attenuation is negligible and the exponential term in Eq. (2.1) can be ignored. Radar backscattering is normally proportional to the sixth power of the diameter of the particles present, favoring the detection of large precipitation particles within a cloud. On the other hand, laser backscattering and attenuation are both proportional to the square of the diameter of the particles present, leading to a greater sensitivity to the presence of all sizes of hydrometeors but also resulting in much stronger attenuation. As a result of the availability of empirically derived relations, microwave scattering theory, and the

Table 2.1 Typical microphysical and scattering parameters for various water clouds.

Cloud Type	h (km)	dh (km)	LWC (g/m^3)	r_m (μm)	N(cm^{-3})	σ (km^{-1})	β' (km/srad)
Stratus	0.1-0.7	0.2-0.8	0.2-0.4	5.5	100-400	30-100	$60\text{-}200\times10^{-3}$
Strato-cumulus	0.6-1.5	0.2-0.8	0.02-0.2	5.0	100-400	3-30	$6\text{-}60\times10^{-3}$
Fog	0	0-0.15	0.05-0.2	2.0	25-800	0.1-20	$0.16\text{-}40\times10^{-3}$
Cumulus	0.5-1.0	0.5-5.0	0.005-0.4	3.5	100-300	10-40	$20\text{-}80\times10^{-3}$

h - cloud base height

dh - cloud thickness

LWC - liquid water content

r_m - mean drop radius

N - drop number density

σ - extinction coefficient

β' - backscatter coefficient

general absence of attenuation, radar is at present a much more useful tool to derive quantitative data.

2.1.4 Multiple Scattering Correction Factor

For water and ice at visible wavelengths, energy absorption is negligible so that optical attenuation can be completely accounted for by the scattering of energy out of the laser beam. One-half of the total energy scattered by a nonabsorbing, large sphere is confined to a narrow cone in the forward-scattered direction (i.e., by diffraction), and this portion of the scattered energy can continue to contribute to the illumination of the target if the receiver beam widths are larger than the rate at which the diffracted component diverges.

The factor η in Eq. (2.1) accounts for this diffracted energy, and ranges between 0.5 and 1.0, depending on particle size and the lidar beam widths used. For example, when looking at rain, most of the diffracted light continues to propagate in the forward direction and does not leave the receiver field of view, so that η approaches 0.5 (Shipley et al., 1974). However, when looking at aerosols with the lidar (i.e., Rayleigh scatterers), there is no diffraction as such, and η would approach 1.0.

2.2 Depolarization in the Backscatter

The laser used in this study emits radiation linearly polarized in the vertical direction. Linear depolarization ratios, or δ values, are calculated to characterize the change in the state of polarization of the energy backscattered from hydrometeors.

The depolarization ratio δ is defined as

$$\delta = \frac{P_{r_\perp}}{P_{r_{||}}} \quad , \tag{2.2}$$

where $P_{r_\perp}$ and $P_{r_{||}}$ are the energies returned in the plane of polarization orthogonal and parallel to that of the transmitted energy, respectively.

Dense cloud layers, composed only of cloud droplets, are easily identified in lidar returns by the presence of near-zero δ values at the cloud base, followed by strong signal increases, evidence for rapid optical attenuation, and δ values which gradually increase with penetration depth. The latter effect is caused by multiple scattering of the laser light among cloud droplets.

The interaction, including scattering and absorption, of an electromagnetic wave incident on a homogeneous sphere larger than the wavelength can be described by using the Mie solution to the Maxwell equation. Generally, energy is backscattered from a sphere through two primary mechanisms: surface waves and paraxial components. For water spheres and light in the visible region, the results of ray tracing methods indicate that the backscattered energy consists almost entirely of rays reflected from the front and rear faces along the axis of symmetry (i.e., the axial rays), while multiple reflected off-axis rays contribute negligibly. It follows that the total axial intensity varies strongly with minute variations in droplet diameter due to ray interference effects.

One problem encountered with the ray tracing method is that it fails to treat circumferentially backscattered energy, that is, the

surface wave. This backscattered wave results when energy becomes trapped at the interface between two dielectrics at or greater than the critical angle of total reflection. For water spheres which are uniformly irradiated, the axial backscatter component is small in comparison to the contribution from surface waves (Liou and Lahore, 1974) as long as the drop remains spherical, but a drop can lose its sphericity.

If drops fall at terminal velocity in the absence of turbulence, they are near perfect spheres if their equivalent radius (r_m) is less than 140 μm. If their radius is $140 < r_m < 500$ μm they become oblate spheroids, and at $r_m = 500$ μm the spheroid develops a flattened base. The flattening becomes increasingly pronounced until near $r_m = 2.0$ mm when a concave base begins to appear. As the drop becomes even larger, the concavity deepens until $r_m \approx 5$ mm the drop becomes unstable and breaks up (Pruppacher and Klett, 1980). In stratus and stratocumulus clouds, the average cloud droplet radius is near 5.0 μm, and the range of drizzle drops is between 50-500 μm. As a result, drizzle drops can become slightly deformed without turbulence and may be a source of some depolarization.

For homogeneous spherical particles (e.g., cloud droplets and small rain drops), the state of linear polarization from *single* backscattering is identical to that of the incident light. However, this would not be true for nonspherical ice particles. Ice crystals, for example, cause a rotation in the incident plane resulting in depolarization due to multiple internal reflections.

The importance of irregular ice particle single scattering cannot

be overemphasized. Some of the largest values occur with large ice particles (e.g., graupel). However, this experiment dealt strictly with liquid phase clouds of >0°C, so ice particle scattering will not be discussed to any great extent here.

Sassen (1977b) measured backscattered laser depolarization in the laboratory from artificially frozen rain drops undergoing the solid to liquid phase change. When the drops began to melt, and were covered by a water shell, the depolarization values were relatively high, almost the same as for pure ice. Even when the water shell continued to increase in thickness and the ice core shrank to the center of the drop, the depolarization values remained high. The optical inhomogeneity of the ice core can provide opportunities for ray paths involving multiple internal reflections. This inhomogeneous particle scattering principle may have an analog in water clouds, as explained below.

During the process of the condensation of a cloud droplet in a maritime environment, the nuclei is likely to be a relatively large salt particle. Newly formed drops would have a salt particle as the condensation nuclei at its core, which would behave similarly to the ice mass in the previous example. Even after the salt particle is mostly diluted in the drop, the gradient in the refractive index of the drop could alter the internal ray paths, perhaps resulting in increased depolarization.

2.3 Multiple Scattering in Water Clouds

2.3.1 Early Laboratory and Theoretical Studies

As previously discussed, it would be expected that no depolarization would result from backscattering by spherical, homogeneous hydrometeors. However, this has not been shown to be the case. Early laboratory studies of artificial water droplet clouds, using continuous wave (cw) laser/lidar analog systems, measured linear depolarization ratios of ~<5% (Schotland et al., 1971; Liou and Lahore, 1974; and Sassen, 1974). It was known that the reason for this depolarization was due to the multiple scattering contribution to the backscattered signal. This invalidates the time-independent scattering assumption, since a large number of photon paths are permissible back to the receiver.

Liou and Schotland (1971) used a computational approach to calculate the δ value from a volume of spherical and uniformly distributed cloud droplets. They used two different cloud models (C4 and C8), representing fair weather cumulus (r_m = 4 μm) and cumulus congestus clouds (r_m = 8 μm), respectively. In both cases the drop number density (N) was set at 100 cm^{-3} and the vertical probe penetration depth was calculated to a depth of 60 m above the cloud base. The receiver beam width was also varied. The maximum δ values were found to vary from 3% at 10 mrad to <1% at 5 mrad for the C4 model, and from 4% at 10 mrad to 2.5% at 5 mrad for the C8 cloud model. In other words, δ values increase as the drop radius increases for a given drop concentration.

Eloranta (1972) used a small angle approximation to calculate the Nth order contribution to a lidar return from a cloud. He calculated δ as a function of penetration depth, and found maximum δ values about four times as large as those predicted by Liou and Schotland (1971), reaching a maximum of approximately 13% at 120 m.

2.3.2 Early Lidar Measurements

Early laboratory studies were useful but could not actually model atmospheric clouds. Usually, a dense cloud had to be created in a small cloud chamber. The cloud had to be dense to make up for the short physical depth of the chamber, which is unlike the situation of a laser pulse penetrating hundreds of meters through a water cloud in the atmosphere. Pal and Carswell (1973) measured backscattered depolarization from cumulus using a ruby laser with 5 mrad beam widths. They found δ values in water clouds that approached 15% in the first 60 m penetration depth, and depolarization ratios of approximately 45% at 150 m. These values were much higher than those predicted by the early laboratory studies or theoretical simulations, prompting new studies to explain these discrepancies.

2.3.3 More Recent Studies

Pal and Carswell (1976) again used cumulus clouds to investigate multiple scattering in the atmosphere. Since multiple scattering leads to depolarization of the incident pulse, and single scattering retains the incident polarization in the backscatter, they investigated the multiple scattered signal by using the depolarization as a tracer. In other words, they separated the contribution of multiple

scattering from the return signal by using the depolarized component. Unfortunately, for the sake of comparison they did not plot δ as a function of penetration depth, but instead used t_m, an attenuation coefficient similar to η, versus the penetration depth. They found that for a cumulus cloud t_m starts at the cloud base with a value close to zero and increases with increasing penetration depth. According to Pal and Carswell (1976), the presence at the cloud base of an extremely low t_m is quite characteristic of low lying cumulus and would indicate the presence of a dilute layer of single scattering spherical particles.

Houston and Carswell (1978) investigated atmospheric clouds using a ruby lidar equipped with a four-channel receiver. This receiver, with a 5 mrad field of view, was capable of independently measuring the four components of the Stokes vectors, I, Q, U, and V. Since δ is a measure of two of the Stokes vectors, they plotted δ versus the penetration depth for a heavy overcast cloud layer with bases near 700 m. They reported a maximum δ value of 17% after an approximately 80 m penetration depth. As far as the other components of the Stokes vector were concerned, Houston and Carswell recommended ". . . that two-channel measurements of δ appear to be the most efficient way to utilize lidar for polarization studies."

In controlled laboratory studies, Ryan et al. (1979) and Sassen and Liou (1979) investigated δ values as a function of the attenuation coefficient and optical depth. Ryan et al. used a set of field stops, placed over the receiver lens, to exclude all single scattered light from the receiver. Upon investigating the dependence of the linear

depolarization ratio versus the cloud attenuation coefficient, they found that depolarization increases rapidly with increasing attenuation, but levels off at δ = 40%. This was attributed to the fact that as the cloud density increases, the depth of penetration of the laser beam into the cloud effectively decreases. The very large δ values can be attributed to the relatively large receiver beam widths (5 and 10 mrad), and to the blocked primary scattering.

Sassen and Liou (1979) also measured δ as a function of cloud attenuation. They found that a linear relationship exists between increases in δ values and optical depth. Using a receiver that viewed a solid angle of 10^{-5} steradians, they measured maximum δ values of ~6% when the extinction coefficient was 3.0 m^{-1}. Their measurements were at θ = 1750, as close to the backscatter direction as possible in the laboratory.

Using a polar nephelometer, they also investigated the angular depolarizing patterns for both water and ice clouds. Upon investigating the relationship between δ and the scattering angle θ for water clouds, Sassen and Liou (1979) found that the maximum δ values of a few percent were in the near-backward direction with the minimum of ~0.1% in the near-forward direction. This demonstrates the effects of diffraction, alluded to in subsection 2.1.4. For spherical homogenoeous particles in the Mie domain, scattering in the forward direction is governed by diffraction and grazing reflections which do not involve any depolarization.

Carswell and Pal (1980) photographed the laser backscattering field from a water suspension of monodisperse polystyrene spheres

through a linear polarizer. They found for sphere sizes in the Mie scattering domain that the backscattered field is highly polarized. When the viewing polarizer has its axes parallel to the incident polarization direction, a cross is formed with maxima in the vertical and horizontal directions. When the polarizer is rotated 90°, to the perpendicular direction, the arms of the cross rotate 45°. Superimposing the two cases would create a complete circle indicating the total backscatter.

Throughout this research, the effect of the receiver field of view was suspected of causing the wide range of values reported. Cai and Liou (1981) used numerical methods to develop a time-dependent transfer model for double, triple, and general multiple backscattering. One of their more significant findings, of importance here, was the effect of the receiver field of view on multiple scattering depolarization ratios. They found that multiple backscattering is significant when the receiver field of view is >10 mrad. Their calculations showed a δ value of 20-30% for a cumulus cloud model when the transmitter beam width and the receiver field of view were 10 mrad, and this was reduced to <5% when for 1 mrad beam widths. Additionally, δ values decrease to <0.2% for a larger transmitter beam width (10 mrad) coupled with a smaller receiver field of view (1 mrad).

Spinhirne et al. (1983) used the lidar from a new vantage point, that of looking down on cloud tops from a high altitude aircraft. Linear depolarization ratios were measured and found to increase with increasing (ice) cloud top heights and decreasing temperatures. Of

more significance to this study was the amount of multiple scattering depolarization obtained by the airborne lidar in low altitude water clouds. The maximum 40-60% depolarization ratios were greater than previously reported measurements or calculations for comparable receiver fields of view (1.5 mrad). The increase was attributed to the increased range factor (15 km versus 1 km) for the airborne observations and the resulting larger beam footprint diameter at the boundary of the scattering medium.

CHAPTER 3

STRATUS CLOUD PROPERTIES

3.1 Cloud Condensation Nuclei

Mixed layers of stratus and stratocumulus clouds are climatologically common over the oceans west of the continents near the location of semipermanent high pressure systems. (For a comparison of typical cloud parameters, see Table 2.1.) Generally, these layers can be divided into two distinct types using the air parcel trajectory and the air mass history. For the purposes of this study, the terms maritime and continental will be used to identify each distinct type.

The main difference between the two types is in the number and chemical nature of the cloud condensation nuclei (CCN). Generally, there is no latitudinal variation in CCN concentration, with continental air masses having more CCN than maritime air masses. The CCN concentration normally decreases with height over the continents. In contrast, maritime CCN concentrations may remain fairly constant with height and sometimes may even increase above the marine inversion (Pruppacher and Klett, 1980).

The different chemical nature of the CCN leads to a difference in cloud droplet spectra n(r) (i.e., number per radius interval) and liquid water content, LWC. Noonkester (1984) measured n(r) in marine stratus layers 110-150 km southwest of San Diego in May and August 1981, and found that the droplet spectra on the days influenced by

continental air contained many more small droplets than on maritime days, a fact also found by Goodman (1977).

Ryan et al. (1972) used an aircraft-mounted particle spectrometer probe to measure cloud droplet distributions in California stratus 30-60 km west of Santa Cruz. As shown in Figure 3.1, although the total droplet concentration (N, cm^{-3}) remains fairly constant, the liquid water content (LWC, gm^{-3}) increases and the drop distribution becomes broader while ascending from the base to the top of the cloud. This cloud was described as a ". . . shallow non-precipitation cloud whose nucleus spectrum is typically maritime."

Goodman (1977) collected data from an instrumented, 250 m high tower located atop a 250 m hill in the center of San Francisco. The coastal stratus was advected onshore by westerly flow, which is similar to the situation at the test site used in this study. In summary, it was found that the drop size distribution was a function of the vertical distance from the inversion base, with the mean diameter increasing with height (see Figure 3.2). Furthermore, the drop size distribution was found to correlate highly with the droplet concentration. Those cases with a high concentration had a narrow spectrum with a well-defined peak and a relatively small mean diameter. That would be expected, since the available water vapor must be distributed over more nuclei. The development of drizzle-sized drops was observed in all cases in the uppermost part of the stratus, and later in the life cycle of the cloud, precipitation-sized drops occasionally reached the ground, as they did in this study.

Goodman concluded that maritime (westerly) trajectories resulted

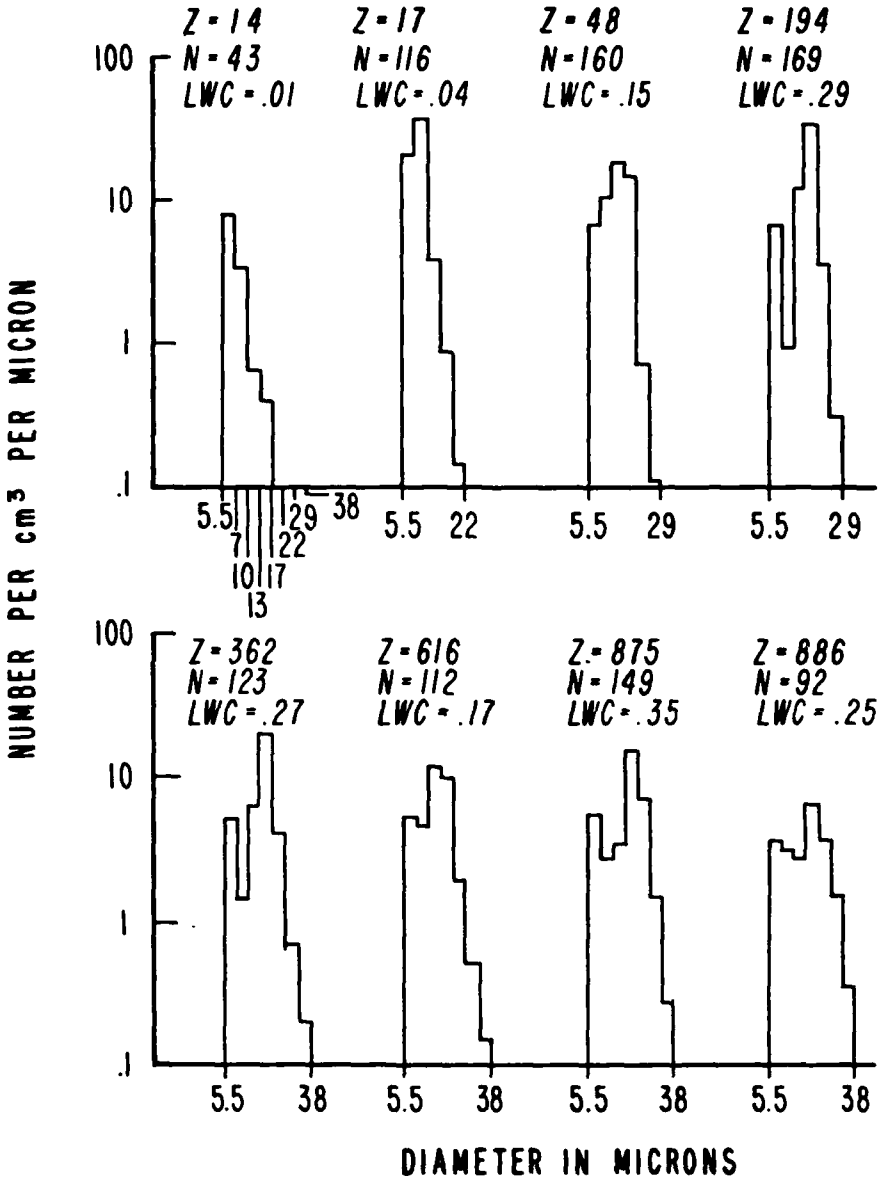

Fig. 3.1 Cloud particle distributions for a gradual ascent through shallow nonprecipitating maritime stratus. Z represents height above cloud base (after Ryan et al., 1972).

Fig. 3.2 Vertical profiles from stratus clouds advected onshore during four periods. Heights relative to the fog top of 1.0 and 0 represent cloud top and base heights, respectively (after Goodman, 1977).

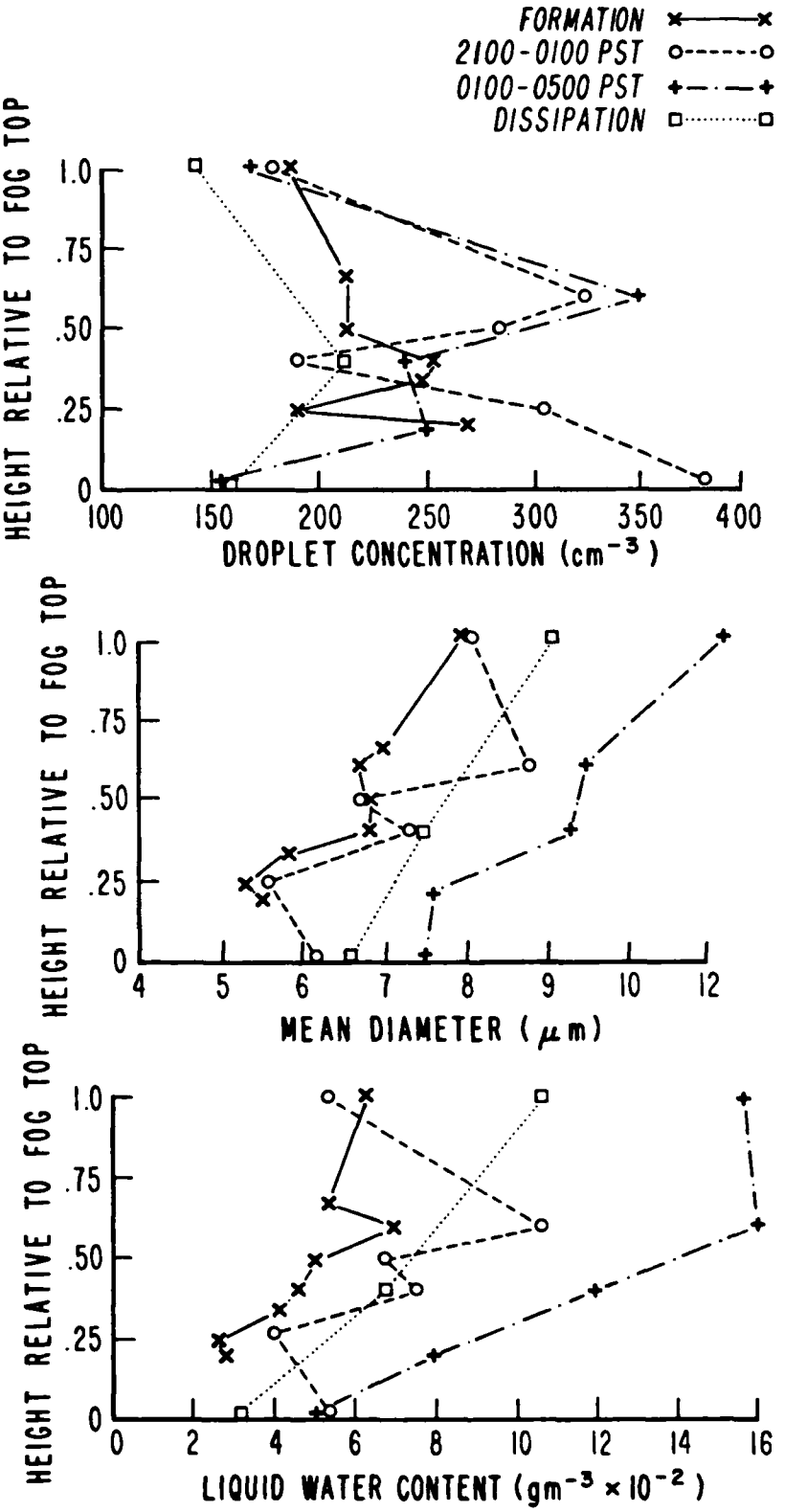
FORMATION
2100-0100 PST
0100-0500 PST
DISSIPATION
HEIGHT RELATIVE TO FOG TOP
1.0
.75
.50
.25
0
100
150
200
250
300
350
400
DROPLET CONCENTRATION (cm⁻³)
HEIGHT RELATIVE TO FOG TOP
4
5
6
7
8
9
10
12
MEAN DIAMETER (μm)
HEIGHT RELATIVE TO FOG TOP
0
2
4
6
8
10
12
14
16
LIQUID WATER CONTENT (gm⁻³ × 10⁻²)

in low droplet concentrations (89 cm^{-3}), large mean diameters, and broad drop size distributions. However, continental (northwest through north) trajectories have higher droplet concentrations (265 cm^{-3}), smaller mean diameters, and narrow drop size distributions with sharper peaks.

3.2 Cloud Water Content

According to Pruppacher and Klett (1980), the distribution of the cloud water content has four characteristic features. Two of these characteristics which are pertinent to this discussion are: 1) the cloud water content increases with height above cloud base, assumes a maximum somewhere in the upper half of the cloud, and then decreases again toward the cloud top; and 2) the distribution of the water content parallels the distribution of the drop size rather than the drop concentration.

The mean LWC measured by Ryan et al. (1972) was 0.20-0.35 gm^{-3}. The liquid water content found by Goodman (1977) was calculated directly from the drop size distributions, and is shown in Figure 3.2.

CHAPTER 4

THE FIELD EXPERIMENT

4.1 Location

The field site was located at San Juan Capistrano, California, at the TRW Corporation test site 185 m above mean sea level (MSL). The experiment dates were June through August 1982. The atmospheric soundings used in this research were taken at Montgomery Field in San Diego, 30 km southeast. These locations are shown in Figure 4.1.

4.2 Equipment

4.2.1 Lidar System

The lidar system consists of a transmitter, a pulsed ruby laser with collimator, and the receiver, a 25 cm diameter telescope. The transmitter and receiver are monostatic, located side by side with parallel axes so that the scattered signal is ~180° with respect to the direction of the incident beam. The entire system is mounted on a table supported by a searchlight mount with manual azimuth and elevation angle control. The mount is on a track inside a van, so that the lidar system can be positioned inside or outside of the van.

The receiver design incorporates a polarizing prism and dual photodetectors to simultaneously measure the components of the returned laser energy. Since multiple scattering strongly depends on the receiver field of view, the receiver beam width can be rapidly

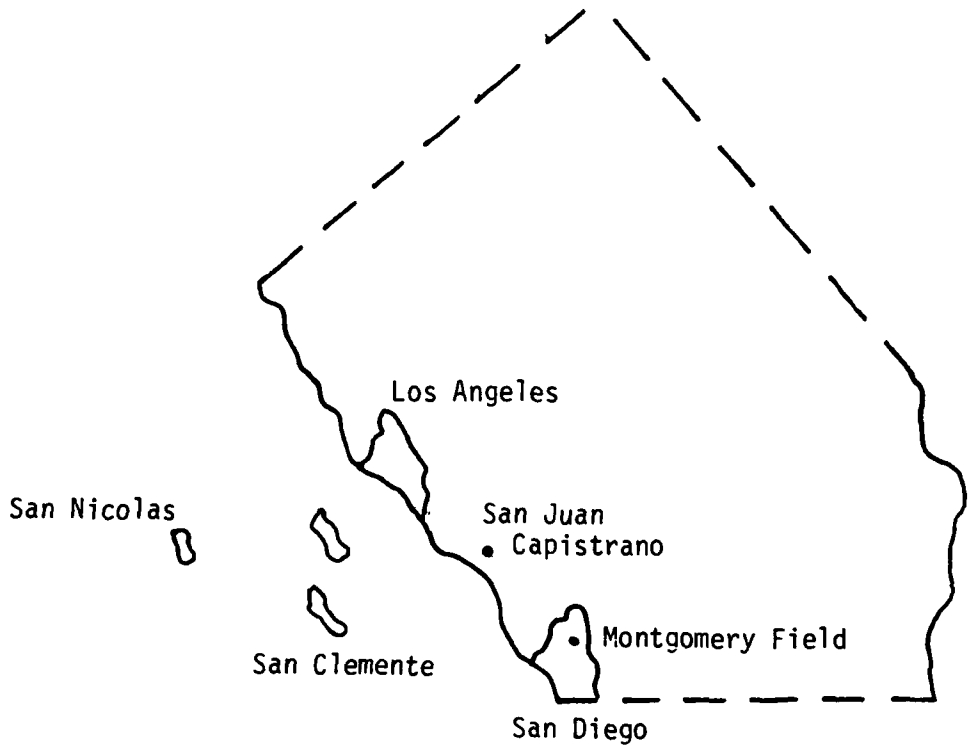

Fig. 4.1 Map of southern California showing the lidar field site and local rawinsonde release locations.

changed. The returned signals are recorded as a function of range on a digital oscilloscope. The complete specifications of the transmitter, receiver, and data handling units are given in Table 4.1.

4.2.2 Lidar Data Collection and Analysis

The lidar data collection and analysis were accomplished using a dual-channel digital oscilloscope with a magnetic disk recorder in combination with a laboratory-based minicomputer. Lidar returns were obtained at 0.25 to 5 min intervals, depending on what particular experiment was being performed, by simultaneously digitizing the parallel and perpendicular polarized signals at a rate of 50 ns per point, yeilding a spatial resolution of 7.5 m in range. The linear depolarization ratios have since been calculated for each pair of data points after compensating for differences in the receiver gain channels determined through a calibration at the field site.

4.3 Synoptic Situation

Discussed in this and the following sections will be some general climatology and the synoptic situation for southern California during the experiment. Included along with these discussions are the National Weather Service (NWS) 1200 GMT surface weather maps, geostationary satellite photographs, and sounding data from the Montgomery Field site.

Southern California generally experiences a Mediterranean type climate characterized by warm to hot summers and mild winters. Cold fronts rarely penetrate this area, with most of the precipitation resulting from moist Pacific air being forced up the slopes of the

Table 4.1 Ruby lidar specifications.

Transmitter	
Wavelength	.694 μm
Energy/pulse	1.5 J maximum
Pulse repetition frequency	0.2 Hz maximum
Pulse duration	3×10^{-8} s
Spatial resolution	4.5 m
Polarization	Vertical
Beam width	1×10^{-3} rad
Receiver	
Aperture diameter	0.25 m
Polarization	Vertical and horizontal
Detector	Dual photomulitplier tubes
Beam width	$1\text{-}3 \times 10^{-3}$ rad, variable
Positioning	Steerable mount
Data Handling	
Digitizer resolution	8 bit (2 channel)
Sample width	7.5 m
Samples/return	2,000 per channel
Sampling rate	20 pulses per minute
Real-time display	Cathode ray tube
Recording	Magnetic disk

Coastal Range. During the summer, as the subtropical high pressure area moves north, extremely stable air moves into the region from the west and northwest, causing widespread stratus, stratocumulus, and fog situations.

4.3.1 Daily Weather Discussion

The NWS 1200 GMT surface chart for 10 June 1982 (see Figure 4.2) shows a low pressure center located near Las Vegas, Nevada with an inverted trough extending along the west side of the Coastal Range in a SE-NW direction. The 500 mb chart indicates convergence over the San Diego area with a moderate southwesterly flow. During the period between 10-14 June, the surface chart showed a continued northerly migration of the subtropical high with most of California dominated by a weak NW-N (continental) flow. On 14 June a weak cold front was located between Los Angeles and San Diego with the 500 mb flow from the northwest. On 15 June there was a return to the pattern established on 10 June, with an inverted trough along the mountains and a low pressure to the east.

4.3.2 Satellite Imagery

The satellite photograph of Figure 4.3 for 10 June 1982 shows a widespread area of stratocumulus extending from the Coastal Range to hundreds of kilometers into the Pacific. In the immediate vicinity of San Diego, the cloud tops appear to be more stratiform, becoming more cumuliform (i.e., cellular) to the west. Other satellite photographs from 14-15 June are remarkably similar to Figure 4.3, although the smoother appearing tops extend further to the west.

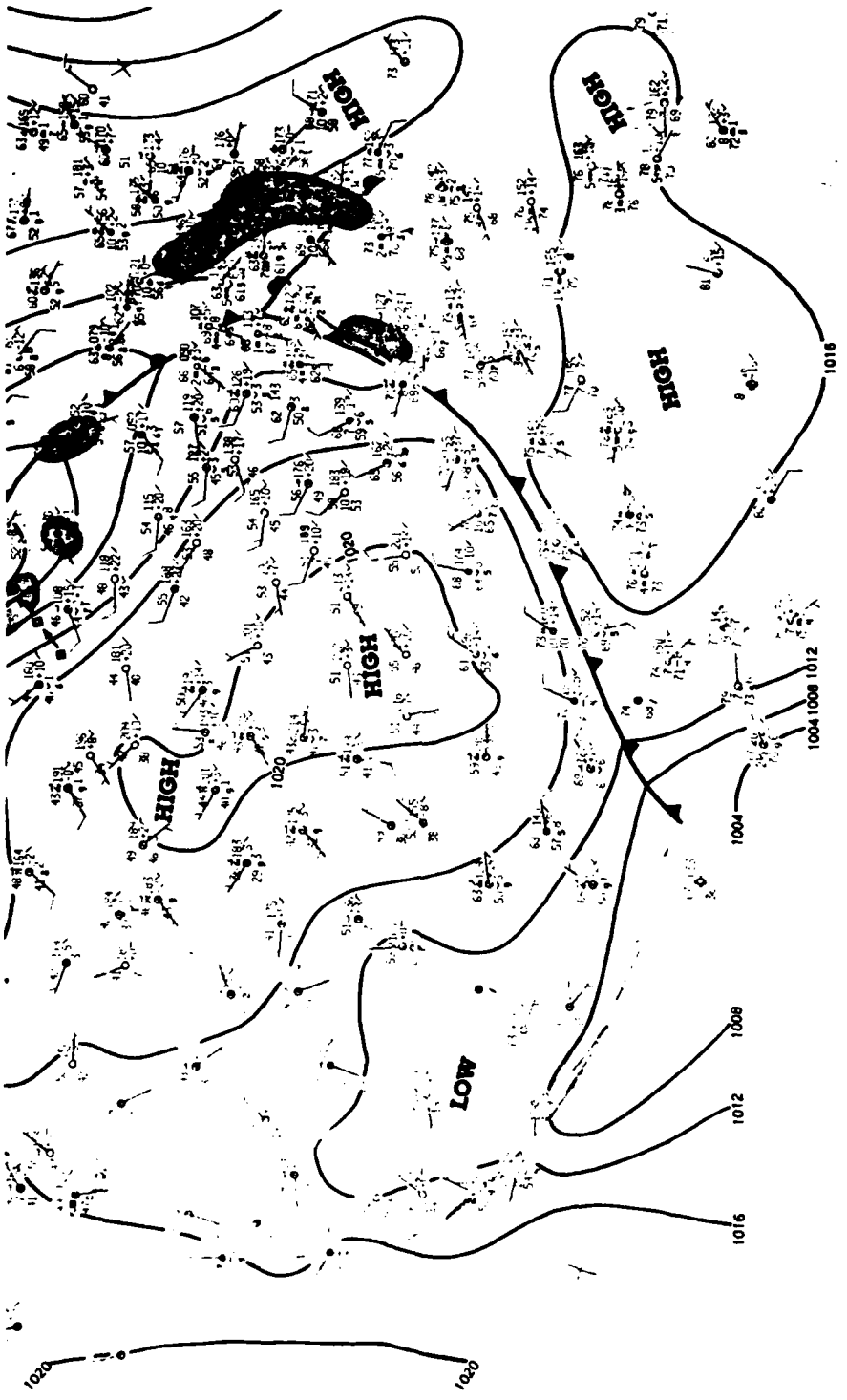

Fig. 4.2 The NWS 1200 GMT surface chart for 10 June 1982.

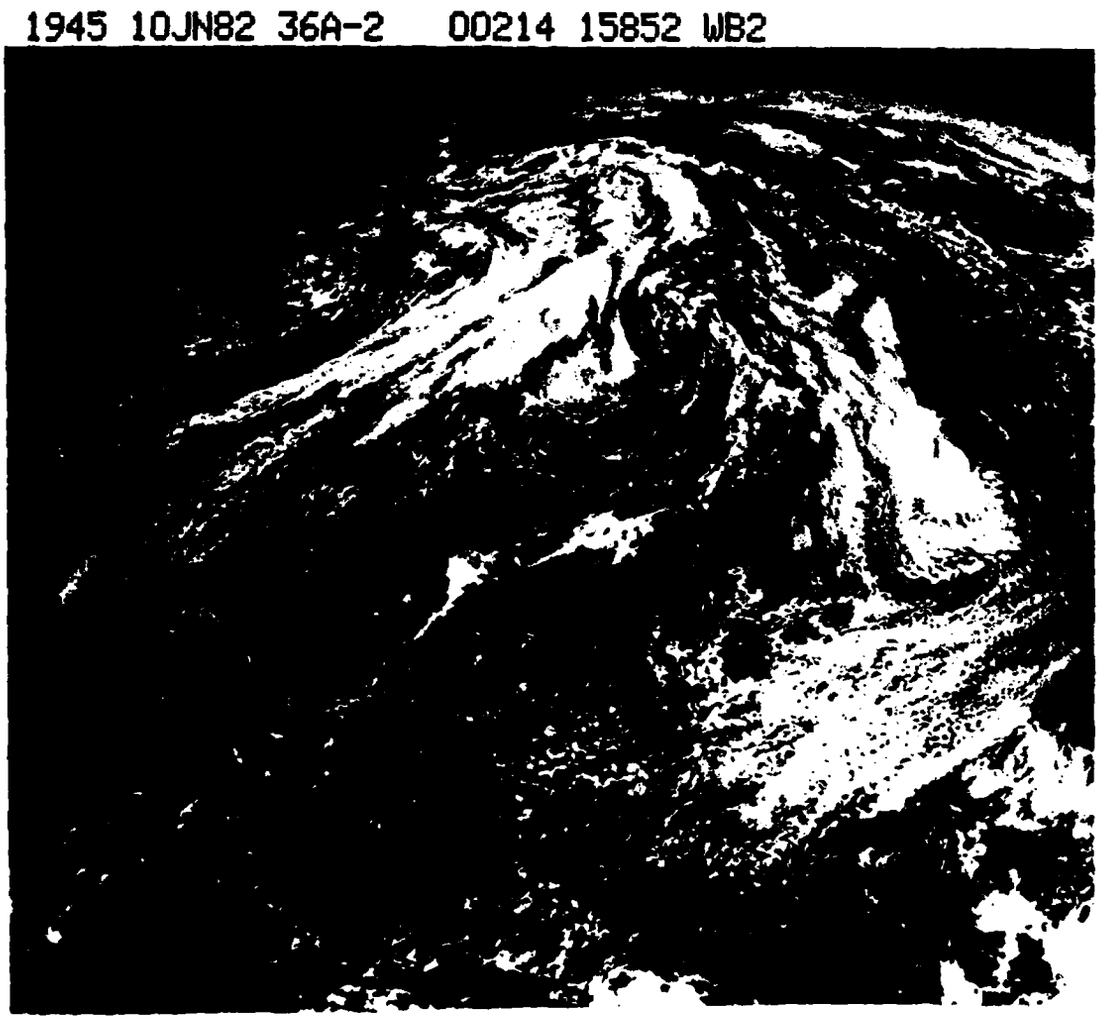

Fig. 4.3 Visible satellite imagery for 10 June 1982 at 1945 GMT.

4.3.3 Atmospheric Soundings

The sounding from 10 June, selected as typical for the observation period, indicates two different inversions above the ground level (AGL) of the lidar field site. The first is a weak frontal inversion between 0.8-1.0 km, with a subsidence inversion present between 1.0-2.0 km. The lifting condensation level (indicative of the cloud base) is at 0.4 km. Above 1.0 km the sounding becomes extremely dry, indicating the upper limit of the cloud layer. Winds throughout the lower 1.0 km are light and westerly and become moderate southwesterlies above the inversion at 2.0 km (see Figure 4.4).

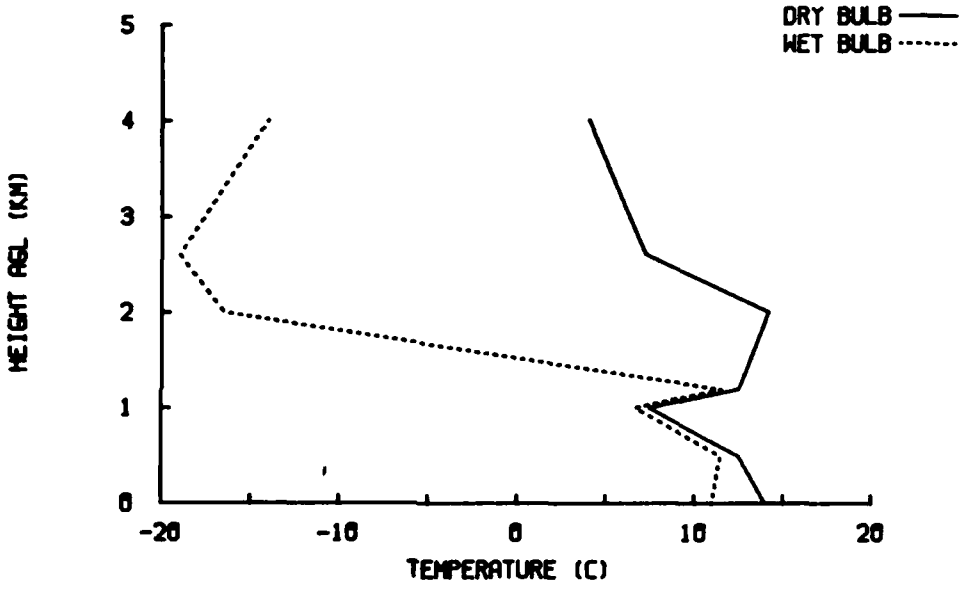

Fig. 4.4 Atmospheric sounding data for the morning of 10 June 1982, from Montgomery Field. The height above ground level (AGL) for the remote sensor site (185 m MSL) is shown.

CHAPTER 5

EXPERIMENTAL RESULTS

5.1 Temporal Variations During Stratus Breakup

The Height-Time (HTI) display of Figure 5.1 shows a layer of stratus undergoing lifing and dissipation on 10 June 1982. The ordinate is divided into hundreds of meters above ground level (185 MSL), and the abscissa is in local time (10 minute increments). The apparent cloud bases and tops are indicated by a solid line and a dashed line, respectively. Areas of strong aerosol returns, apparently left over from cloud dissipation, are indicated by short dashed lines. Linear depolarization ratio intervals, in percent, are shaded and identified in the key, and range from near 0 to 22.4%. All of the data for this HTI were obtained at a 90° elevation angle, using a 1 mrad receiver field of view.

Before continuing with the discussion of the HTI, a discussion of how the cloud base was determined is warranted. When referring to the cloud base from the atmospheric sounding data, the height of the lifting condensation level (LCL) was used. The LCL is the height at which a parcel of air becomes saturated when lifted dry adiabatically. When referring to the lidar cloud base, a determination has to be made as to the exact definition of a cloud base. Since the lidar signals are affected by the air molecules and the cloud condensation nucleus activation zone beneath a cloud layer, the backscattering

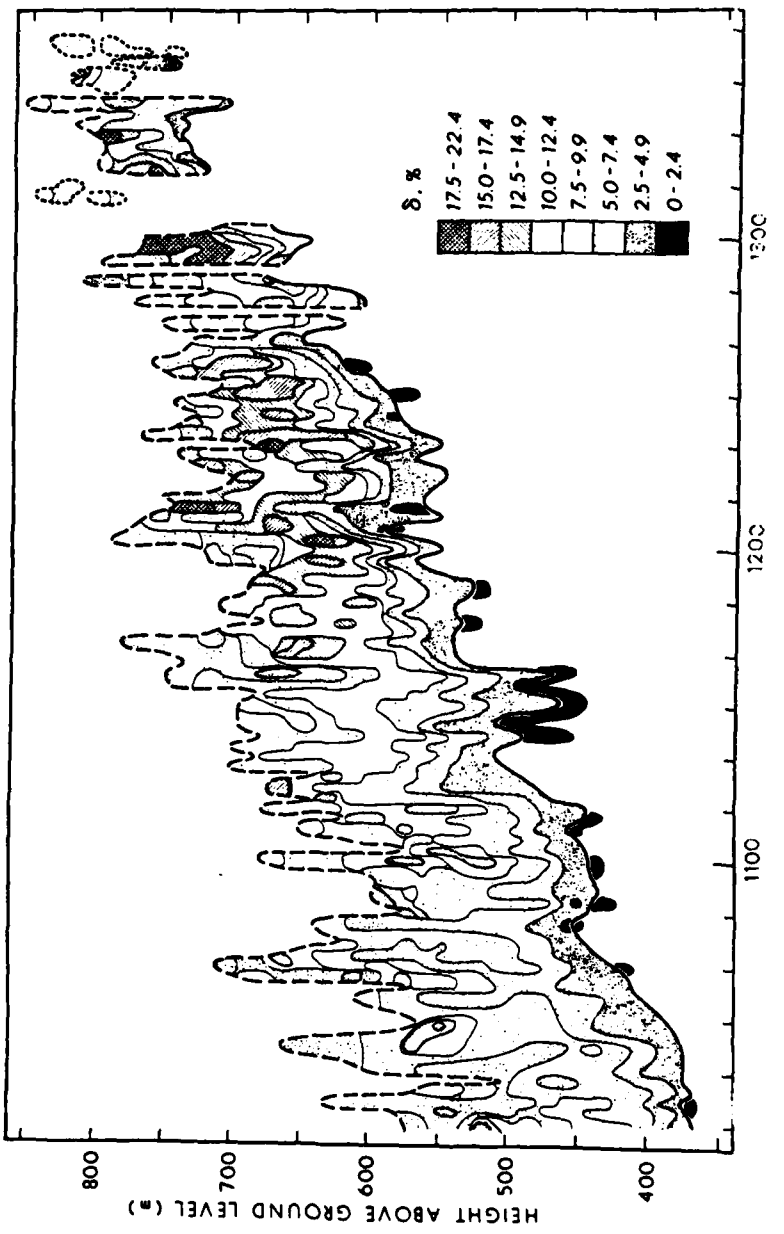

Fig. 5.1 Height versus time display of lidar δ values during the dissipation of a stratus layer at the indicated times on 10 June 1982.

signals typically begin to increase below the level corresponding to 100% relative humidity, particularly in the maritime environment. For this experiment, the cloud base was defined as the height at which the first of three consecutive 10% parallel-polarized energy increases were measured in the digitized signals.

5.1.1 Visual Cloud Observations

Since optical surface observations were unavailable for this specific location, it will be helpful to describe the visual observations of the stratus layer during dissipation.

At 1130 LT (Local Time), the lidar operator reported a "ridged" stratus overcast with intermittent drizzle occurring. Thirty minutes later a few blue patches appeared before returning to the overcast condition. At 1240 LT the operator reported that the sun was visible with 7/10 cloud coverage, and at 1310 LT, 4/10 "cumulus-type" clouds decreasing to 2/10 coverage at 1330 LT were reported.

5.1.2 Lidar Findings

At the beginning of the time period, between 1010-1030 LT, the stratus cloud base was indicated at approximately 375 m, with ragged tops extending to approximately 600 m above ground level (AGL). The cloud top heights shown in Figure 5.1 may not represent the actual top of the layer, however, due to the attenuation of the laser pulse. However, the maximum cloud heights roughly agree with the sounding data for this occasion.

A good agreement exists between the operator's observations, the lidar measurements of the stratus layer, and the cloud heights

derived from the atmospheric sounding of Figure 4.4, which indicated a possible cloud layer between 0.4-1.0 km AGL. Throughout the period, the stratus layer lifted with intermittent drizzle occurring, especially at 1130 LT. At that time, the lidar indicated a depolarization value of <2.4% below the cloud base. A value this low could only be due to spherical, homogeneous droplets at relatively low concentrations. In other words, light drizzle was indicated below the cloud base. The effect of multiple scattering or depolarization under these conditions is minimal due to the 1 mrad receiver field of view. The period after 1240 LT indicated a break-up of the stratus layer with holes between the cloud elements. The periods near 1310 LT and 1335 LT indicated an enhanced aerosol return, probably attributable to the dissipation of the stratus clouds. This area had a depolarization value less than the surrounding cloud elements, but greater than the weak aerosol returns below the cloud base (generally between 2.5-7.5%) which have been omitted from the figure.

Above the cloud base, the value of the depolarization ratio typically increases rapidly with increasing penetration depth. Higher in the cloud, however, the δ value variations are clearly more erratic with position and time. This is due to multiple scattering effects, coupled with cloud microphysical content variations. Some of the microphysical variations to be expected in this cloud layer during dissipation can be seen by referring to Figure 3.2 (after Goodman, 1977).

Figure 3.2 shows the properties of a stratus layer covering the period from formation to dissipation. It illustrates that the liquid

water content and mean drop size distribution have increasing values with height and time until reaching the dissipation stage. Then the values for both LWC and drop size decrease below the maxima attained in the middle stages. The droplet concentration has no noticeable trend except for a pronounced decrease in the upper portion of the cloud layer.

The relation of these general cloud properties to the depolarization data is unclear, but early in the period shown in Figure 5.1, when the apparent cloud depth was large, the range of δ values was small, only 2.5% to 10%. However, as the cloud layer appeared to thin, the range of δ values increased from 2.5% to 17.5%, with the largest area of high δ values occurring at 1300 LT when δ reached values between 17.5% and 22.4%. Cloud composition changes and the increasing distance to the target may both have contributed to the increasing δ values from multiple scattering with time and height.

5.2 Receiver Beam Width Effects

Throughout this research, the effect of the lidar receiver beam width has been identified as a major contributing factor to depolarization ratios due to multiple scattering in water clouds. As reported earlier, water clouds were probed with lasers, modeled, numerically simulated, and found to have δ ratios as low as a few percent to as high as almost 50%. The receiver field of view was ususally different from one experiment to the next, ranging from 10^{-2} rad to 10^{-4} rad. Even though different results for the same beam widths have been reported, no study has systematically varied the receiver beam width and used the lidar in the atmosphere to

measure the backscattered depolarization from water clouds. The following nine figures represent the first time that this has been accomplished (Figures 5.2 - 5.10).

These figures, from 14 June, will be divided into groups according to the lidar elevation angle. They were selected as typical examples from a sample of approximately one hundred lidar returns for this day. There are four figures at 90°, three at 60°, and one each at 50° and 30°. Most of these figures depict the linear depolarization ratio (in %) as a function of vertical penetration depth (m) above the cloud base, and compare 1 mrad and 3 mrad receiver fields of view. Beneath each δ value plot is the corresponding graph of the relative returned energy in the parallel polarization plane, given in arbitrary units. Unlike the HTI data display of Figure 5.1, which has the appearance of an actual cloud layer, these figures are derived from single lidar pulses and resemble the A-scope displays available in real time from most modern radar or lidar systems.

In Figure 5.2, instead of using the penetration depth above cloud base, the depolarization ratios and relative returned energies are shown as a function of height above ground level. These have been added to illustrate the apparence of a lidar return through the atmosphere from the surface to approximately 600 m. The specific numerical values from this figure are not important at this time, but an understanding of what the lidar senses and how that will be displayed is important. This figure shows a low altitude aerosol plus molecular return and a stratus cloud return beginning at 500 m AGL for both 3 and 1 mrad receiver fields of view. The rapid increase in

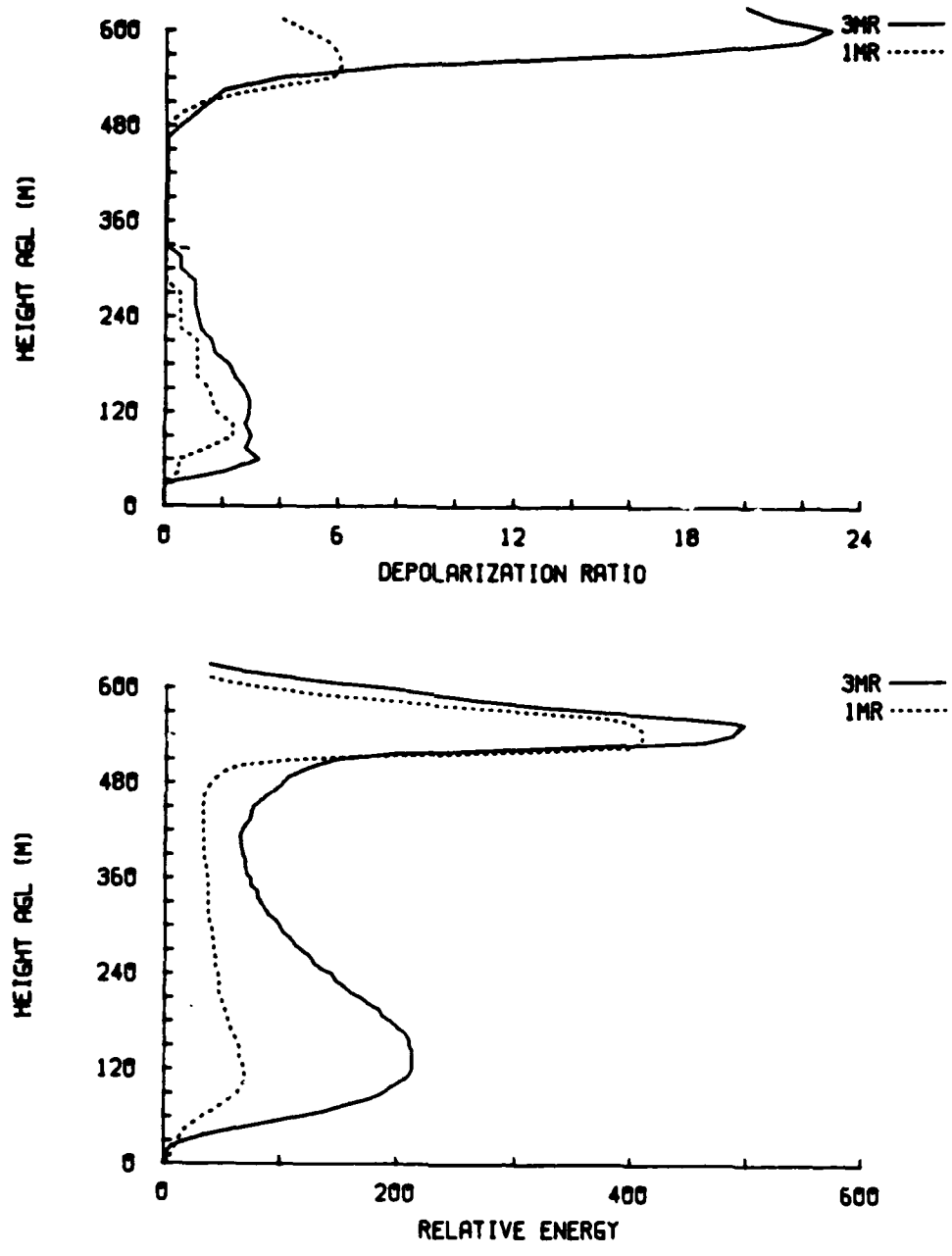

Fig. 5.2 Linear depolarization ratio (in %) and relative returned energy (in arbitrary units) profiles plotted as a function of height above ground level for two consecutive lidar pulses using 1 and 3 mrad (MR) receiver beam widths. The lidar elevation angle was 90°. The data were collected at 1036 LT on 14 June 1982.

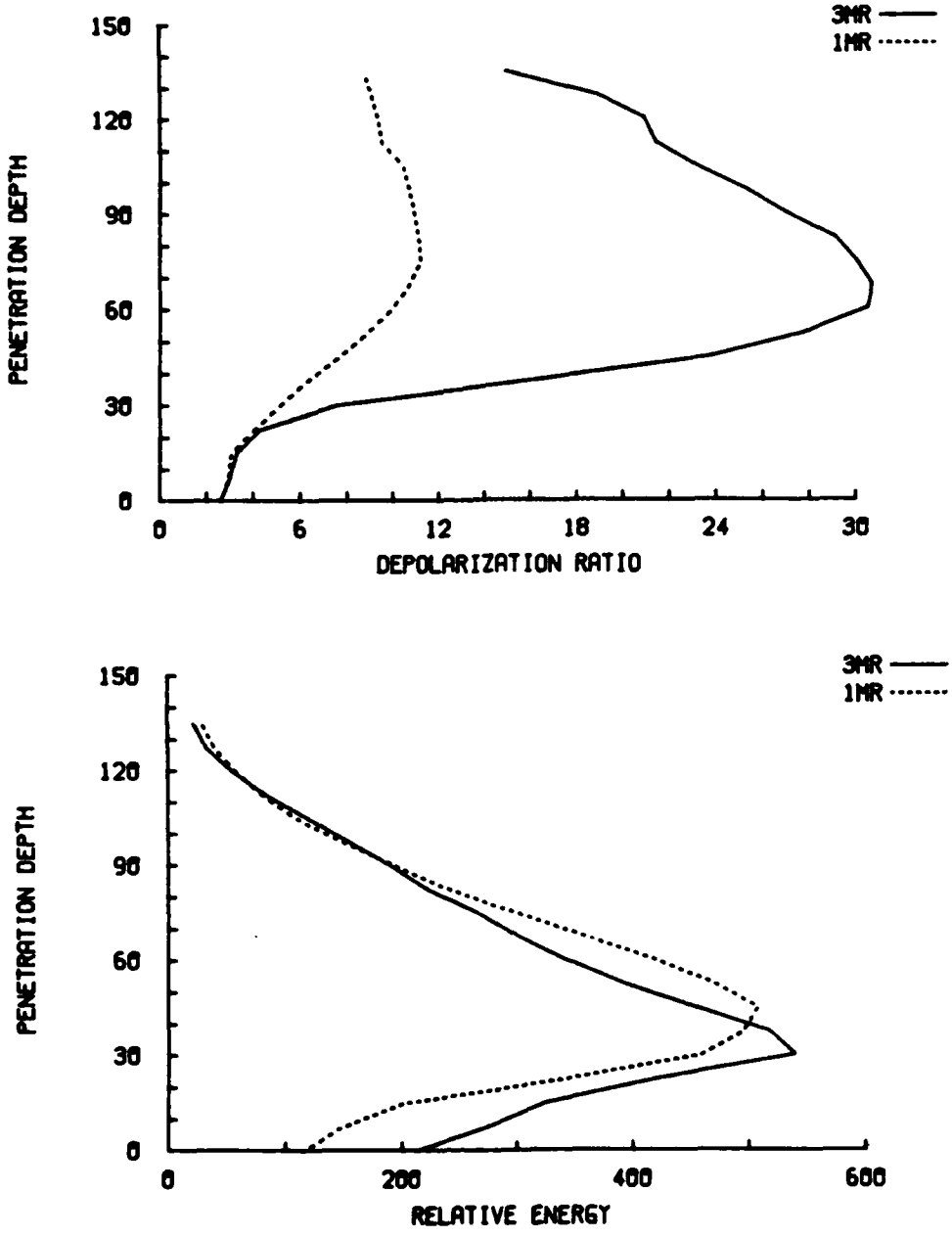

Fig. 5.3 Linear depolarization ratio (in %) and relative returned energy (in arbitrary units) profiles plotted as a function of vertical penetration depth above cloud base for two consecutive lidar pulses using 1 and 3 mrad (MR) receiver beam widths. The data were collected at a 90° elevation angle at 1234 LT on 14 June 1982 from a cloud with a 480 m cloud base.

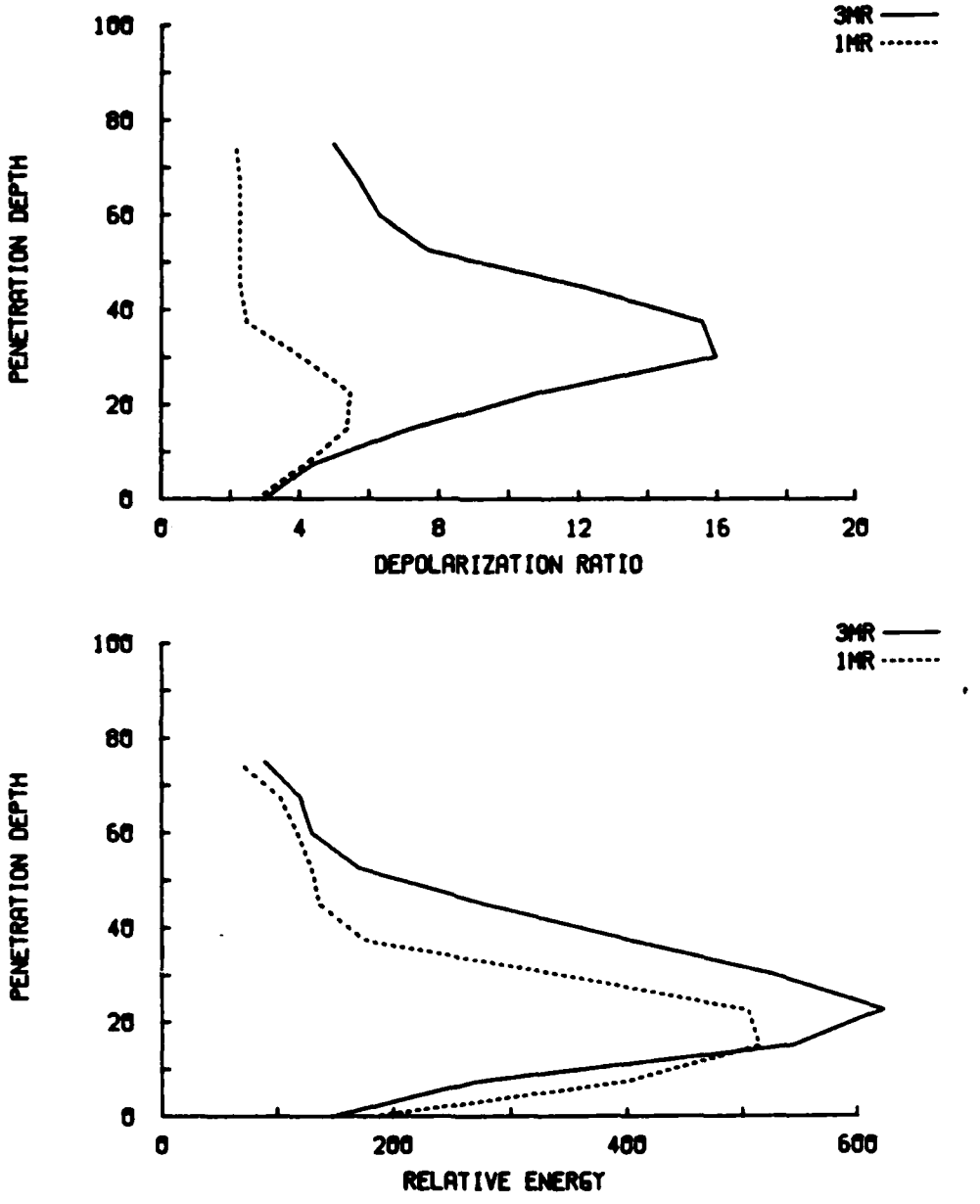

Fig. 5.4 Linear depolarization ratio (in %) and relative returned energy (in arbitrary units) profiles plotted as a function of vertical penetration depth above cloud base for two consecutive lidar pulses using 1 and 3 mrad (MR) receiver beam widths. The data were collected at a 90° elevation angle at 1259 LT on 14 June 1982 from a cloud with a 480 m cloud base.

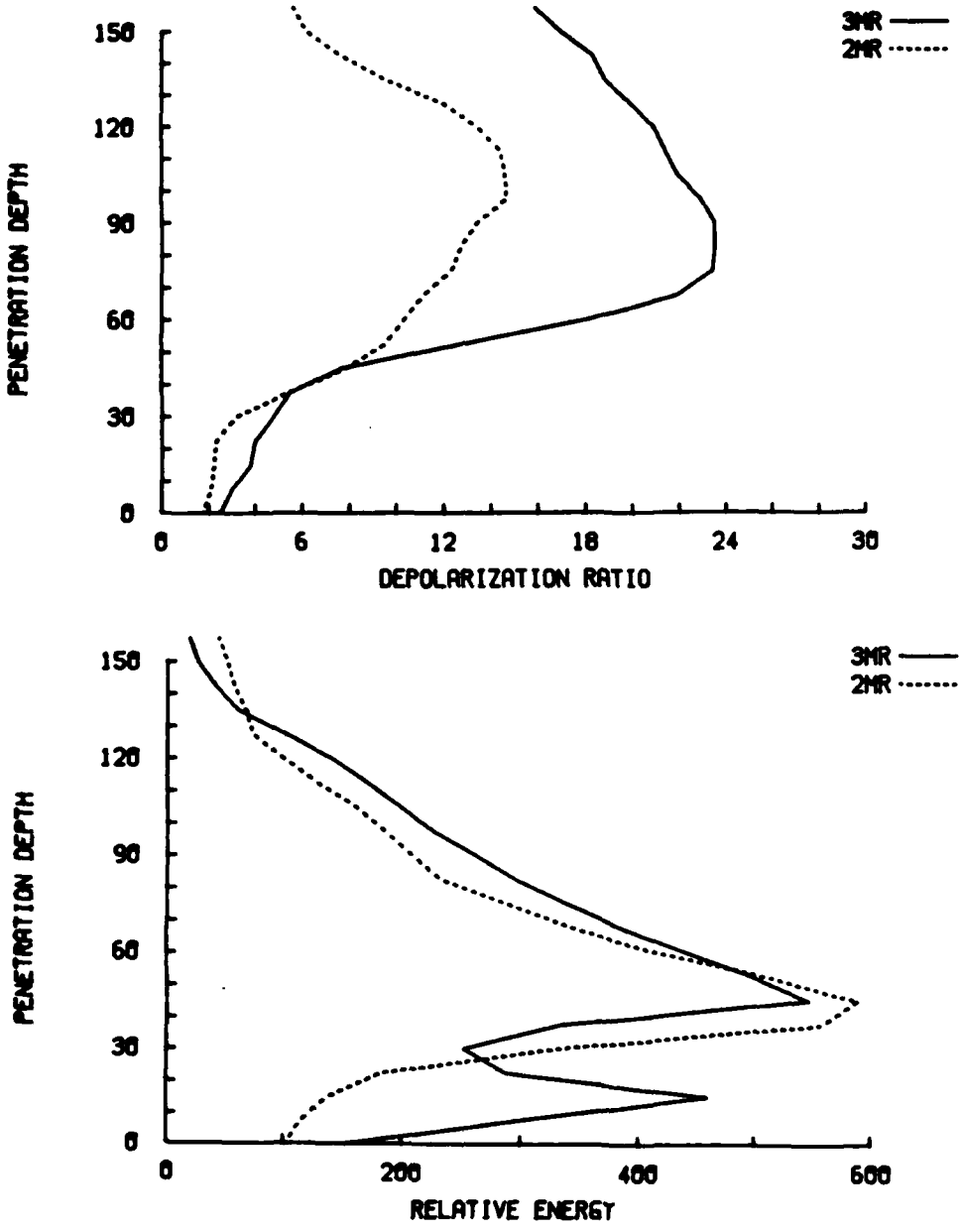

Fig. 5.5 Linear depolarization ratio (in %) and relative returned energy (in arbitrary units) profiles plotted as a function of vertical penetration depth above cloud base for two consecutive lidar pulses using 2 and 3 mrad (MR) receiver beam widths. The data were collected at a 90° elevation angle at 1355 LT on 14 June 1982 from a cloud with a 510 m cloud base.

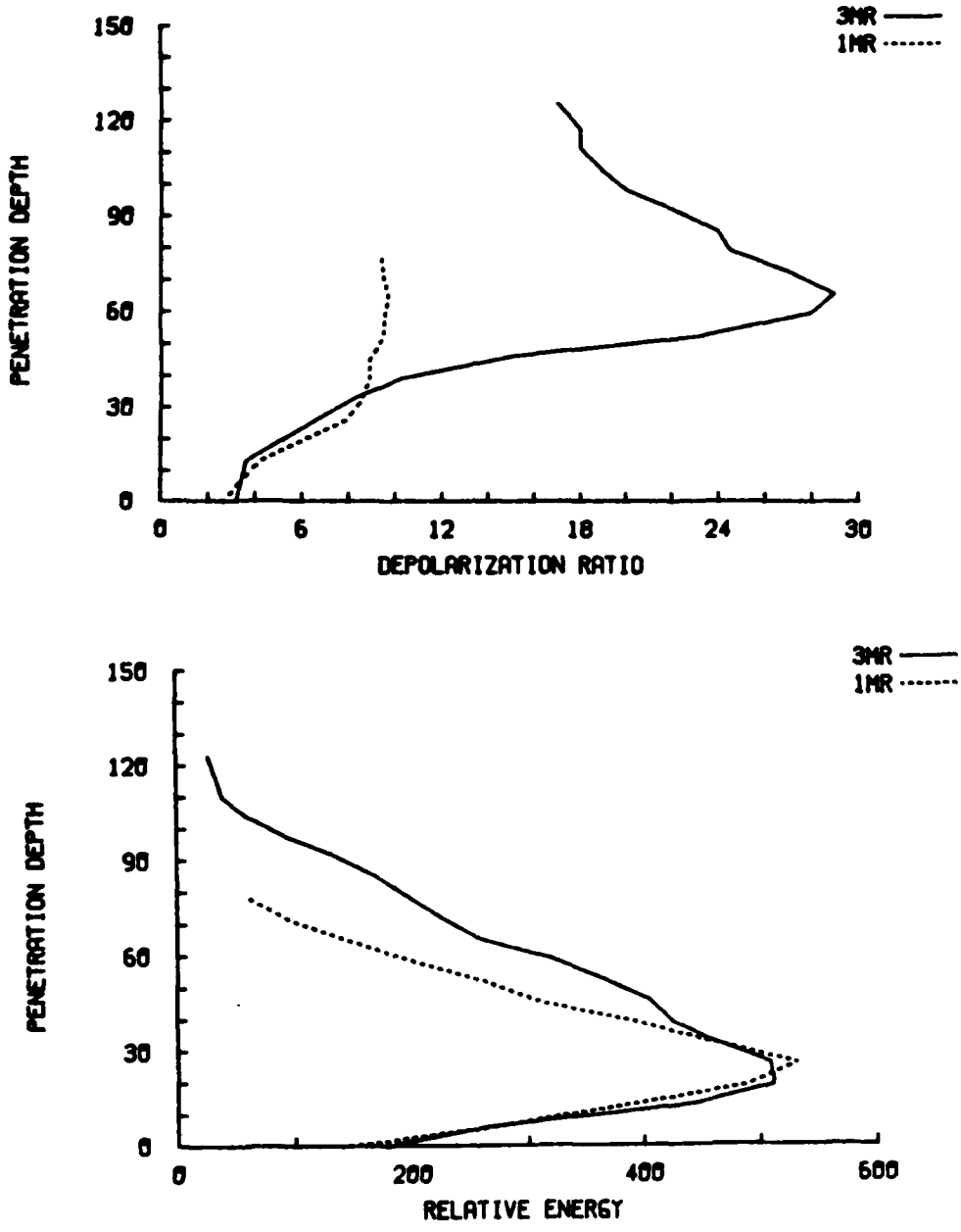

Fig. 5.6 Linear depolarization ratio (in %) and relative returned energy (in arbitrary units) profiles plotted as a function of vertical penetration depth above cloud base for two consecutive lidar pulses using 1 and 3 mrad (MR) receiver beam widths. The data were collected at a 60° elevation angle at 1124 LT on 14 June 1982 from a cloud with a 450 m cloud base.

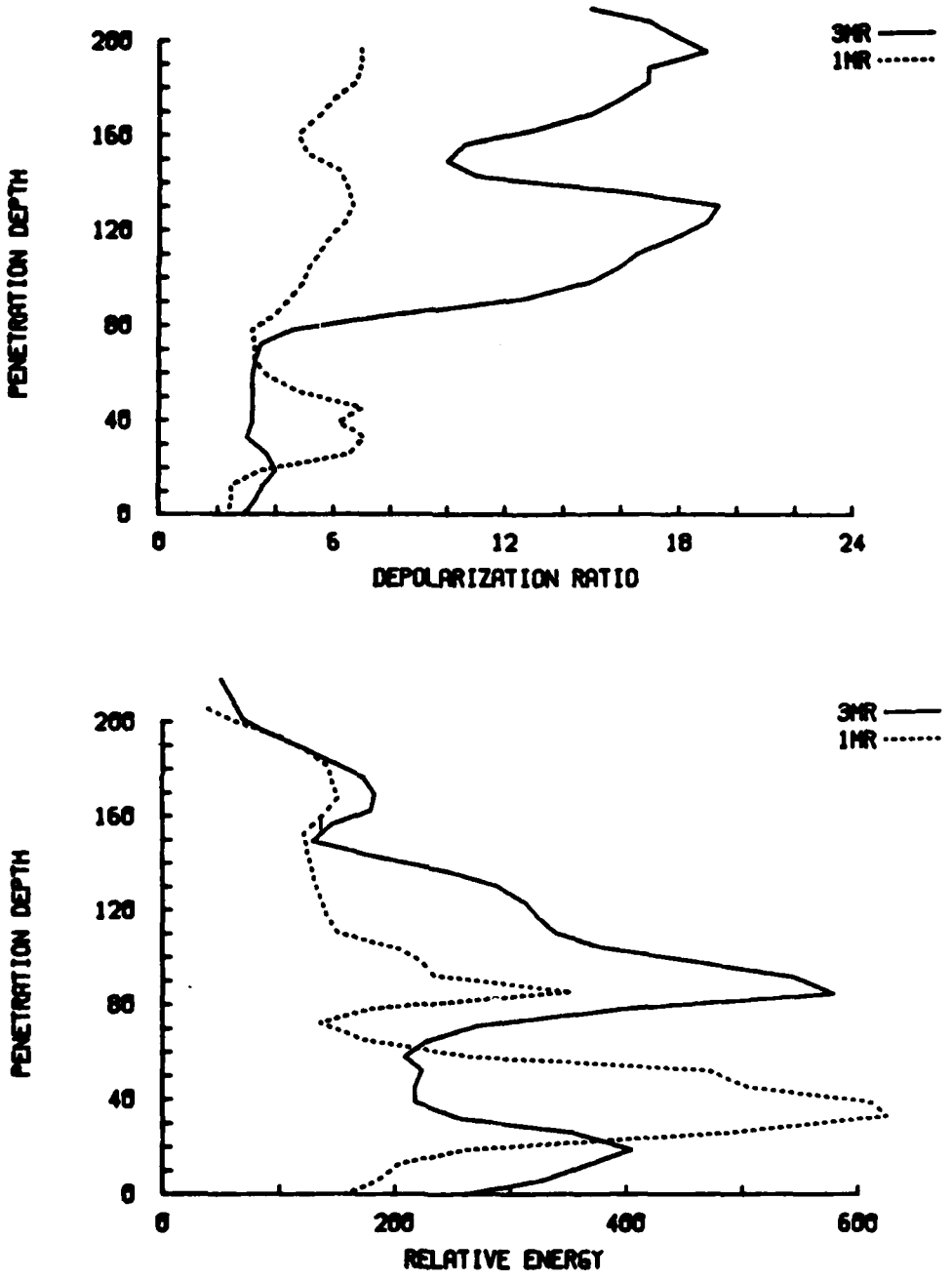

Fig. 5.7 Linear depolarization ratio (in %) and relative returned energy (in arbitrary units) profiles plotted as a function of vertical penetration depth above cloud base for two consecutive lidar pulses using 1 and 3 mrad (MR) receiver beam widths. The data were collected at a 60° elevation angle at 1217 LT on 14 June 1982 from a cloud with a 410 m cloud base.

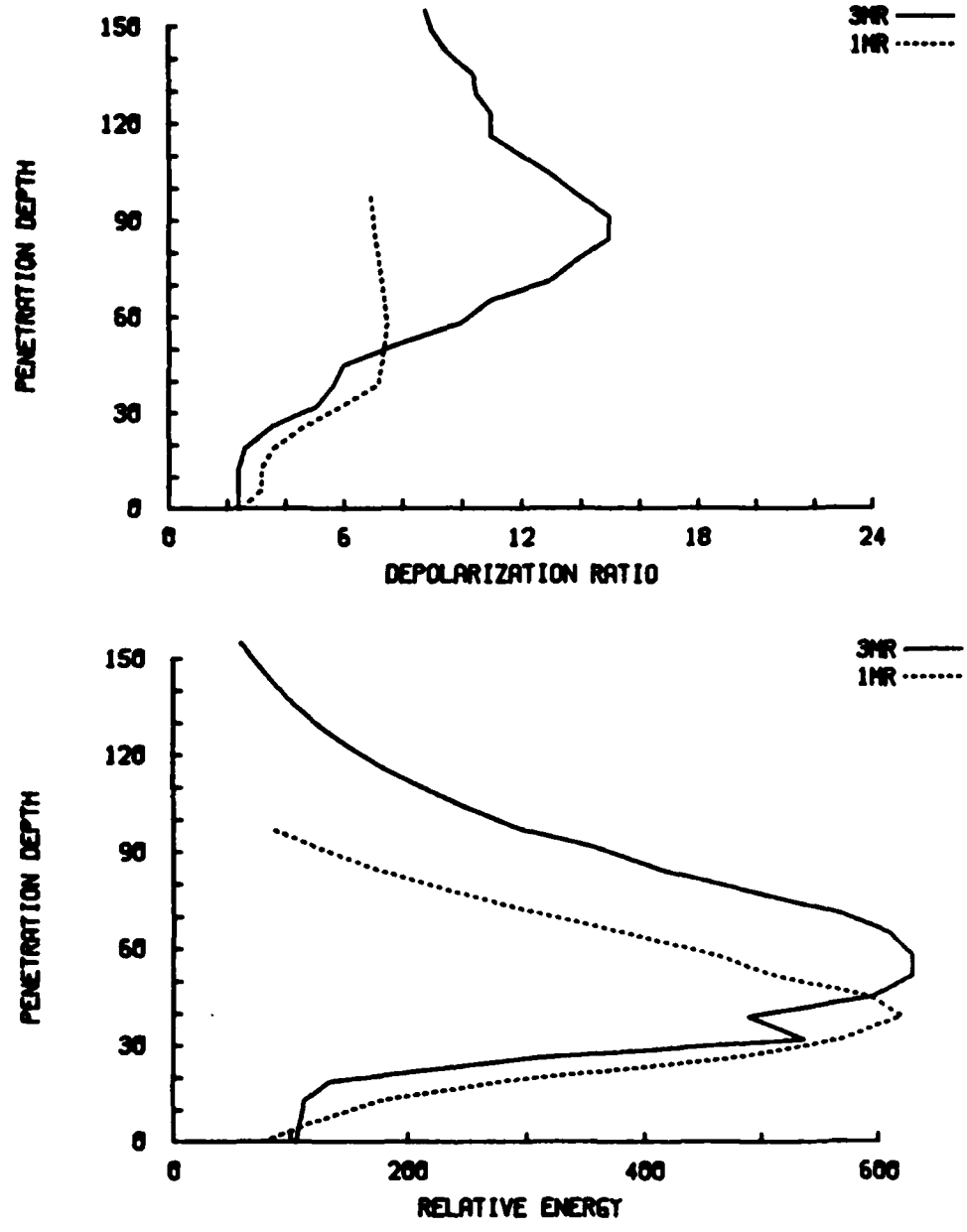

Fig. 5.8 Linear depolarization ratio (in %) and relative returned energy (in arbitrary units) profiles plotted as a function of vertical penetration depth above cloud base for two consecutive lidar pulses using 1 and 3 mrad (MR) receiver beam widths. The data were collected at a 60° elevation angle at 1448 LT on 14 June 1982 from a cloud with a 630 m cloud base.

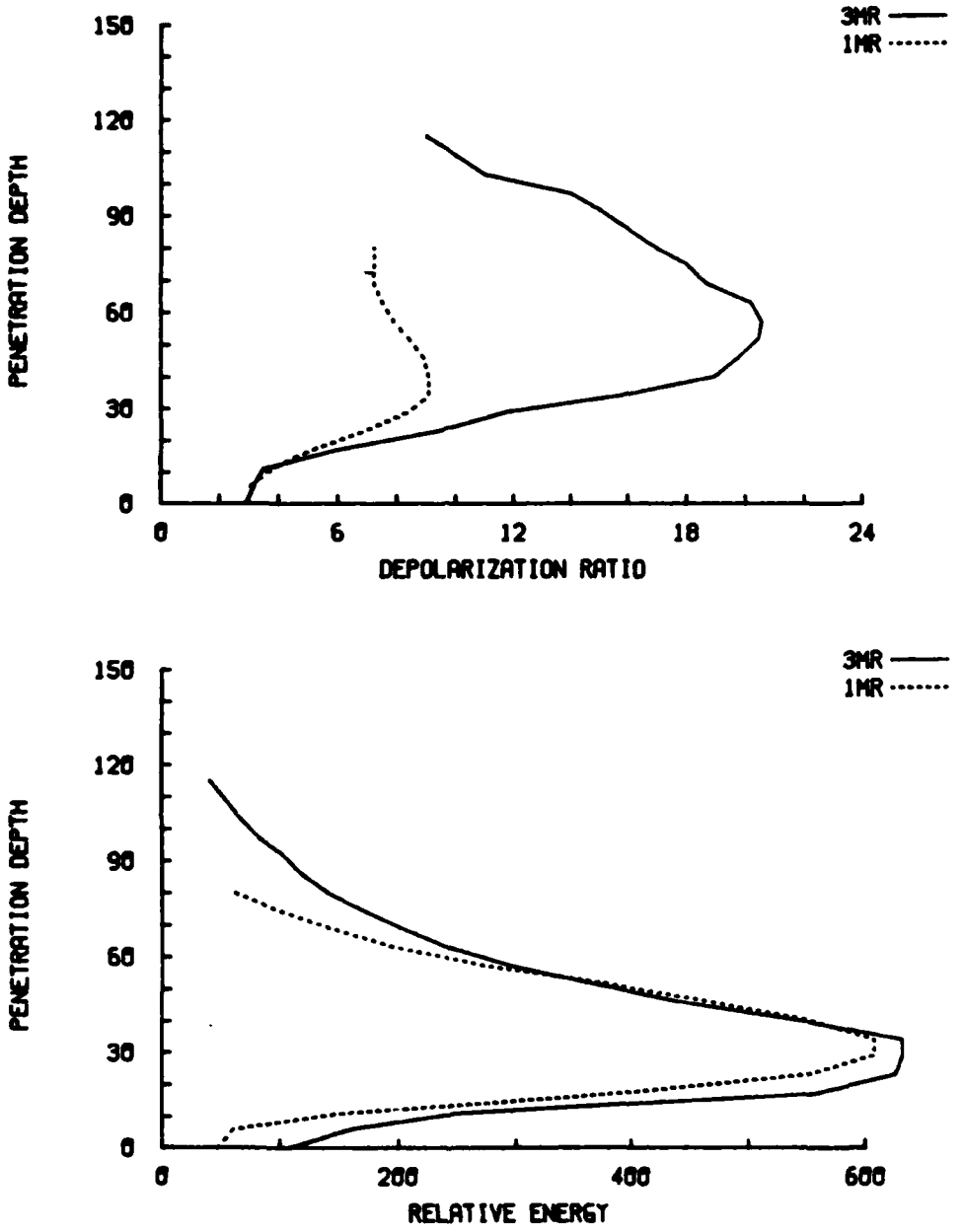

Fig. 5.9 Linear depolarization ratio (in %) and relative returned energy (in arbitrary units) profiles plotted as a function of vertical penetration depth above cloud base for two consecutive lidar pulses using 1 and 3 mrad (MR) receiver beam widths. The data were collected at a 50° elevation angle at 1511 LT on 14 June 1982 from a cloud with a 580 m cloud base.

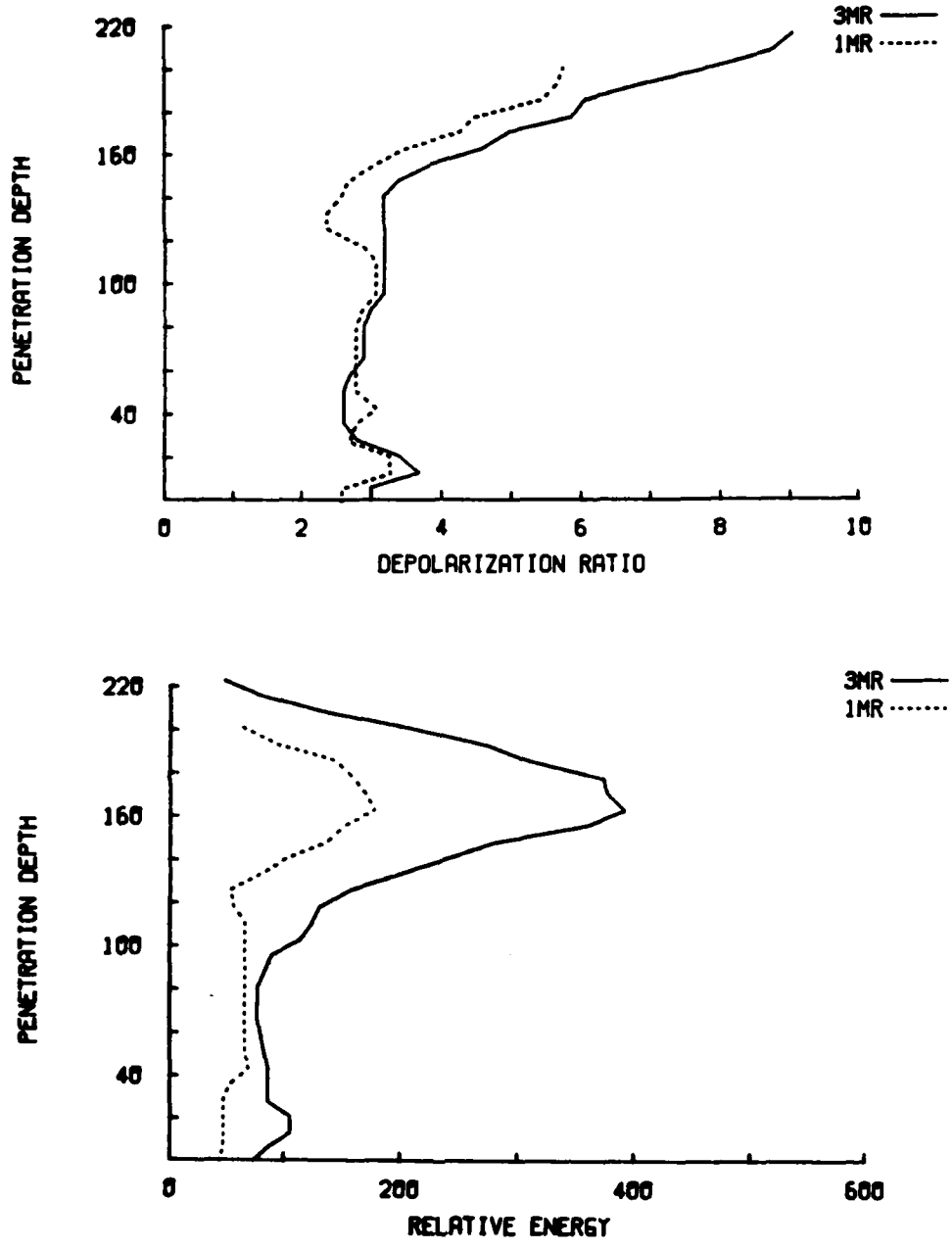

Fig. 5.10 Linear depolarization ratio (in %) and relative returned energy (in arbitrary units) profiles plotted as a function of vertical penetration depth above cloud base for two consecutive lidar pulses using 1 and 3 mrad (MR) receiver beam widths. The data were collected at a 30° elevation angle at 1418 LT on 14 June 1982. The penetration depth scale begins at 540 m AGL.

returned energy below 120 m, the point at which the transmitter/ receiver beam widths overlap with this lidar (see Section 2.1.2), is indicative of multiple scattering among air molecules and aerosols. Above this level the returned energy tends to decrease due to the inverse range-squared law, until a gradual and then sudden increase marks the cloud nuclei activation zone and the strong cloud base return. Another notable feature pertains to the depolarization ratio. It is significantly higher for the 3 mrad as opposed to the 1 mrad field of view, as will be considered in the next section.

5.2.1 Observations at a 90° Elevation Angle

To begin the discussion of the variable beam width data collected on 14 June 1982, Figure 5.3, from 1234 LT, shows a maximum depolarization ratio about three times as large for 3 mrad (31% versus 11%) as for 1 mrad. Figure 5.4, obtained 25 minutes later, also shows a trebled δ value for the 3 versus 1 mrad receiver beam widths (5.5% versus 16%). This was the rule for most of the approximately one hundred cases reviewed for this day. When comparing the 3 versus 2 mrad data in Figure 5.5 (1259 LT), the maximum δ values are nearly doubled. The maximum relative returned energy varies roughly between 500-600 (arbitrary units), with the 3 mrad returns generally having a higher peak value than 1 mrad. In Figure 5.5, a double cloud layer may have been encountered, since the relative energy returned increased at 20 m and then decreased before increasing again at 30 m.

Maximum depolarization values at a 90° elevation angle on this day ranged from 16% to slightly over 30% at 3 mrad, and between 6% and 15% at 1 mrad. It is apparent that these data would fall somewhere

in the middle of the ~5% to 50% range reported earlier in laboratory, theoretical, and atmospheric measurements.

5.2.2 Observations at a 60° Elevation Angle

Figures 5.6, 5.7, and 5.8 are from 1124 LT, 1217 LT, and 1448 LT, respectively. For each of these figures the slant range of the pulse into the cloud was converted to a vertical penetration depth above the cloud base scale through the use of the sine law. As at the 90° elevation angle, maximum δ values are two to three times greater for the 3 mrad as opposed to the 1 mrad observations. One characteristic at the 60° elevation angle is that δ reaches its maximum value lower in the cloud for 1 mrad than for 3 mrad, and usually maintains this value until the signal drops off. This was not the case at 90°, where the δ profiles for both 1 mrad and 3 mrad were more bell shaped. At a lower elevation angle, the laser beam takes a longer path to reach the same height in the cloud as a result of its slant path. Since the composition of the cloud would be expected to change above the cloud base, lidar returns varying as a function of elevation angle would also be expected.

5.2.3 Observations at 50° and 30° Elevation Angles

The example of a 50° elevation angle return in Figure 5.9 again has an almost threefold increase for the depolarization ratio between 3 and 1 mrad. The shape of the 1 mrad δ profile has a definite peak, as in the 90° returns, but the δ values do not continue to decrease as the signal decreases.

The unusual set of lidar returns given in Figure 5.10 is for 30° elevation angle observations collected at 1418 LT. Figure 5.10 has approximately the same δ values for both 3 and 1 mrad up to ~100 m penetration depth, which are due to the presence of a weak subcloud layer probably containing cumulofractus clouds. The depolarization ratio and relative energy profiles both indicate a much stronger scattering cloud layer. Unfortunately, there were no other observations performed at 30° at this time.

5.3 Elevation Angle Effects

In the previous sections, elevation angle effects naturally entered into the description of the receiver beam width effects. However, the time between the observations at various elevation angles was often quite large, making it difficult for intercomparisons. For the next three figures, the time between shots varies only by minutes, so the elevation angle effects can be more closely compared.

Figure 5.11 compares 90°, 60°, and 30° elevation angle observations collected with a 3 mrad receiver beam width at 1427 LT, 1429 LT, and 1431 LT, respectively. The patterns discussed in the previous sections still hold true for these figures. For example, maximum depolarization values and relative returned energy peaks tend to be reached lower in the cloud as the angle is decreased.

Figure 5.12 is given to assess the temporal variability of the data shown in Figure 5.11. These data were collected one minute later at each angle. Both figures are very similar, showing the conservative properties of the stratus layer and the lidar system over a

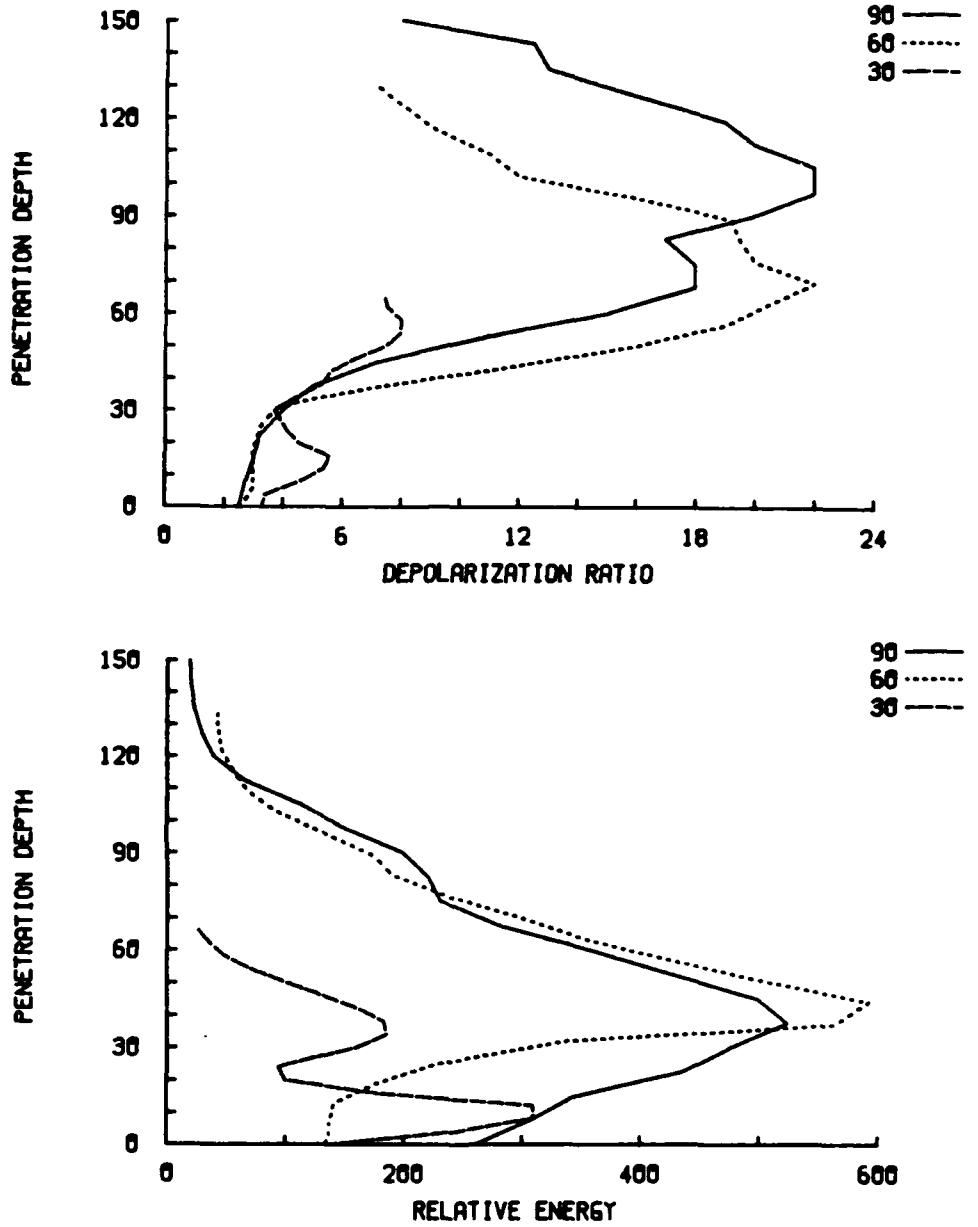

Fig. 5.11 Linear depolarization ratio (in %) and relative returned energy (in arbitrary units) profiles plotted as a function of vertical penetration depth above cloud base for 3 mrad observations taken 2 min apart at the indicated elevation angles. Average cloud base was at 545 m AGL.

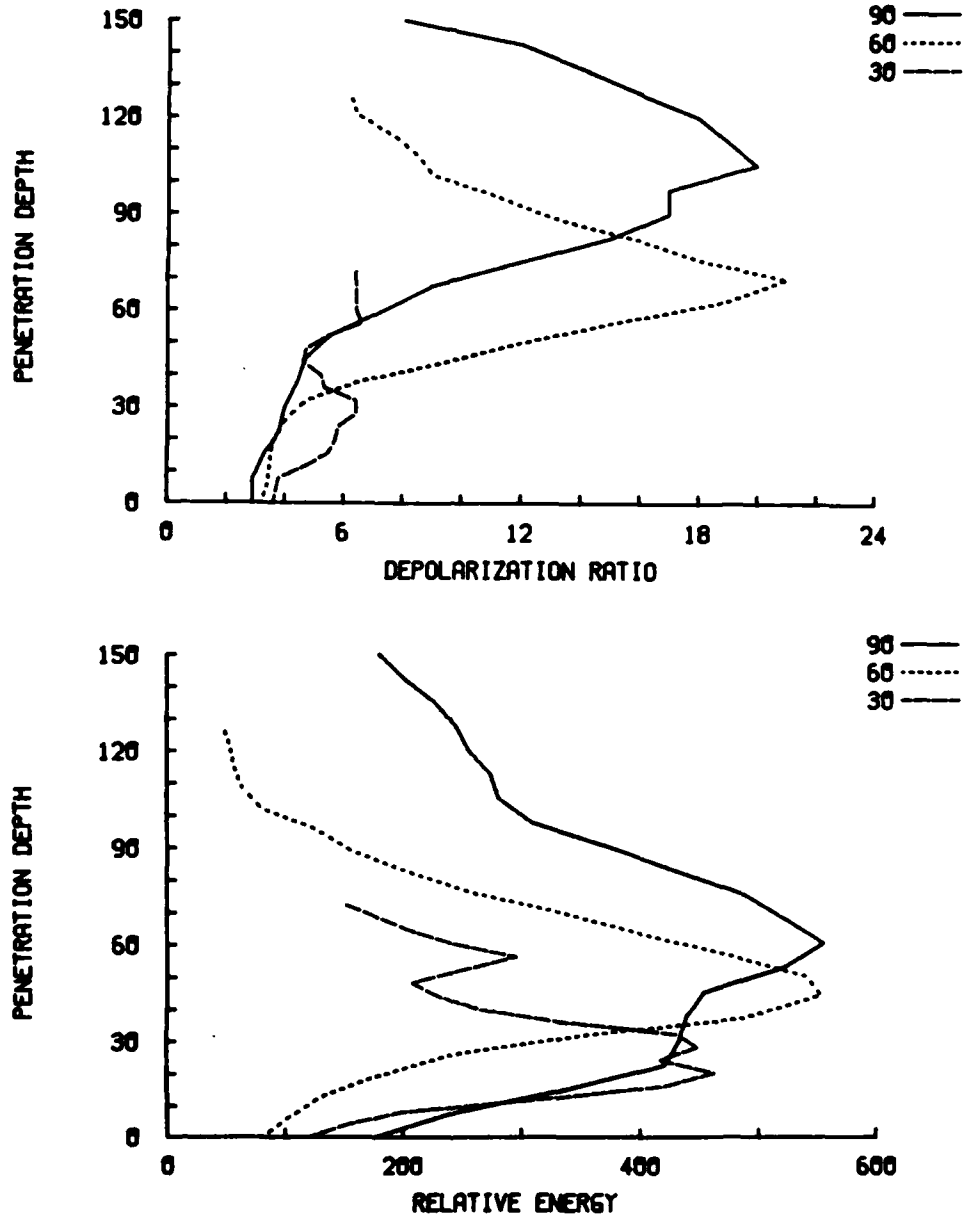

Fig. 5.12 Linear depolarization ratio (in %) and relative returned energy (in arbitrary units) profiles plotted as a function of vertical penetration depth above cloud base for 3 mrad observations taken 2 min apart at the indicated elevation angles. Average cloud base was at 545 m AGL. The data were collected one minute later at each elevation angle than in Figure 5.11.

short time period.

Figure 5.13 presents the data in Figure 5.12 as a function of slant path range into the cloud. It can be seen that both the maximum δ values and the relative energy peaks more closely coincide when using the slant path distance as opposed to the vertical penetration depth above cloud base. However, the dissimilar δ values in the cloud between the 90° or 60° and 30° data point to the presence of cloud microstructure changes as a function of distance above the cloud base.

5.4 Beam Misalignment Effects

This section of the experimental results deals with the deliberate misalignment of the lidar transmitter and receiver axes. As mentioned in Section 2.1.2, the transmitter and receiver axes must be aligned in parallel by sighting a fixed target through the telescope while steering the laser pulse with the collimator. To test the effect of misalignments, the laser beam alignment was deliberately moved off-axis with respect to the transmitter. Figure 5.14 shows the effect of this misalignment, and was taken at matched 1 mrad beam widths with a 45° elevation angle. The beam axes were made to diverge in steps starting from an angle of 0.0 (the aligned case) to 7.5 mrad off alignment in the vertical direction.

For the 0.0 mrad return of Figure 5.14, a cloud layer is indicated between 320 and 400 m with a maximum δ value of about 5%. As the off-axis misalignment increases to 0.9 mrad, the returned laser energy begins to decrease and a small increase in the δ value is noted. However, the next step (2.0 mrad off-axis) and each successive

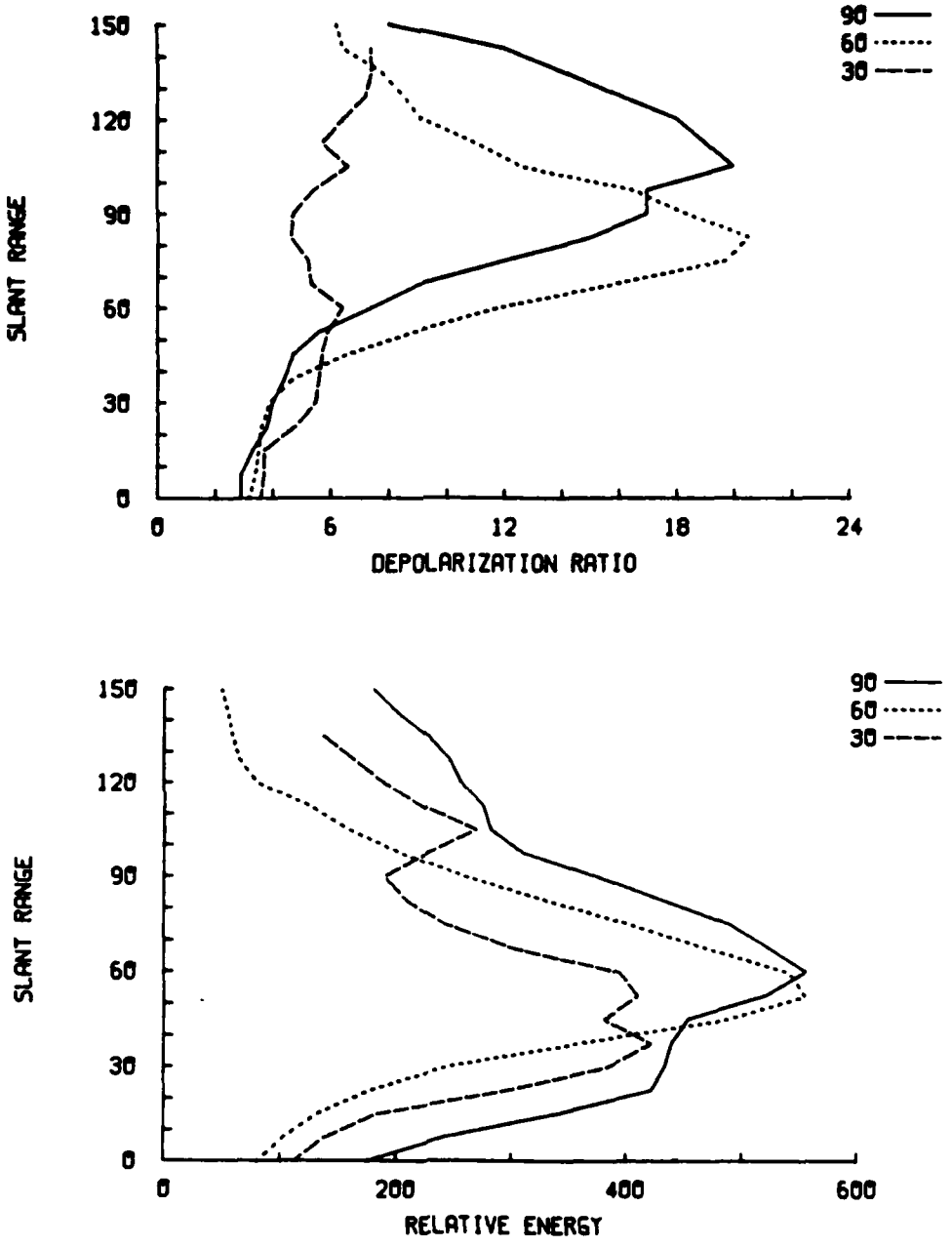

Fig. 5.13 Linear depolarization ratio (in %) and relative returned energy (in arbitrary units) profiles plotted as a function of slant path range into the cloud for 3 mrad observations taken 2 min apart at the indicated elevation angles. Average cloud base was at 545 m AGL. The data were collected one minute later at each elevation angle than in Figure 5.11.

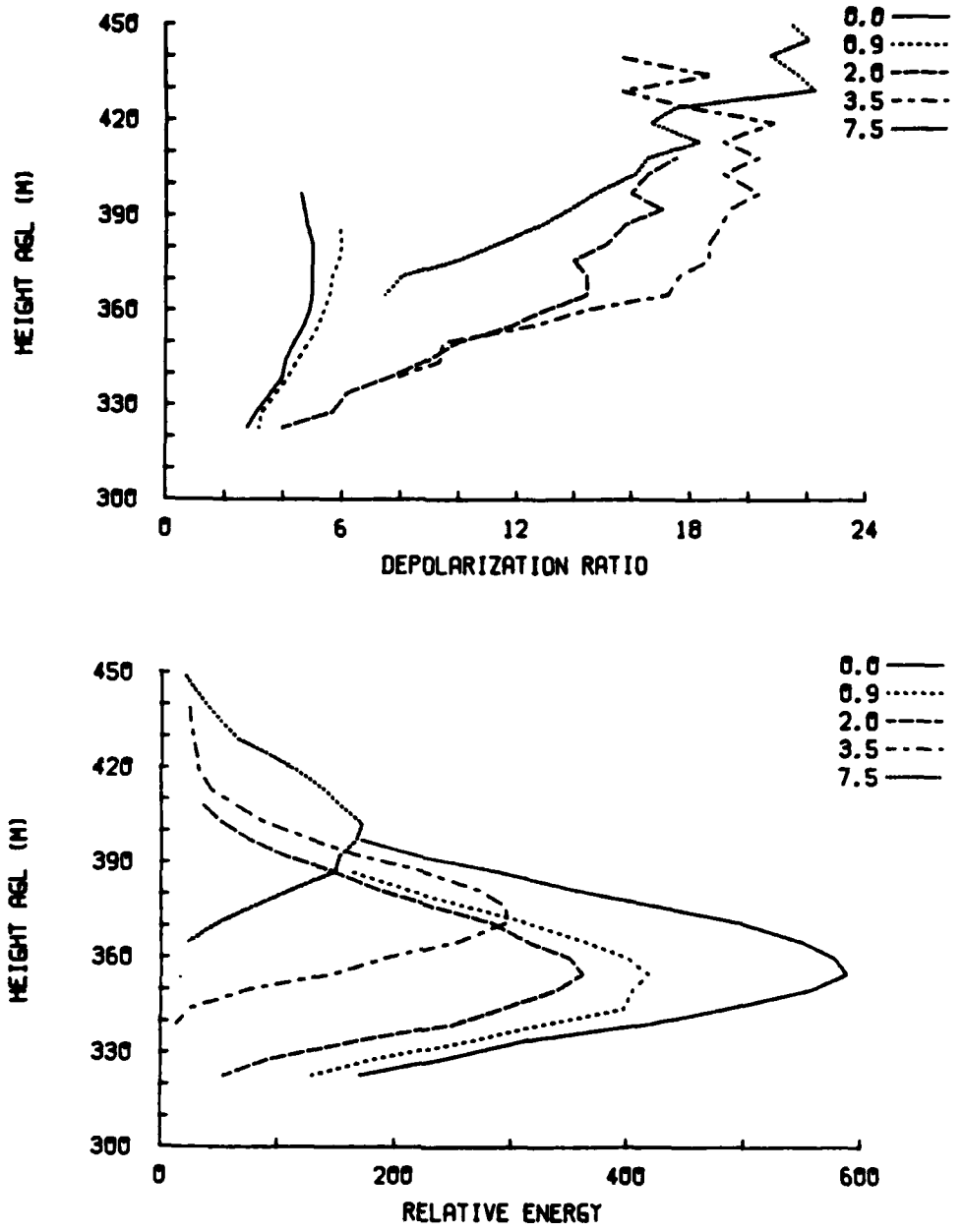

Fig. 5.14 Effects of transmitter/receiver beam misalignment on returns from a stratus cloud layer with a cloud base at 320 m above ground level. Numbers in the keys refer to receiver pointing angle misalignment, in mrad. The elevation angle was 45°.

step thereafter shows a dramatic change. As the angle of misalignment increases, the transmitter and receiver beams increasingly fail to overlap, and the detection of multiple scattered energy is increasingly favored over single scattering. Eventually, the return is due only to multiple scattering.

Regarding the relative energy portion of the figure, the energy peak returned decreases for each successive off-axis plot and moves further up in the atmosphere. It appears that as the beams move further apart progressively higher orders of multiple scattering are detected by the receiver. These observations illustrate the time-dependent nature of the multiple scattering process, since the cloud layer appears to move to higher altitudes with increasing misalignment.

CHAPTER 6

CONCLUSIONS

The overall purpose of this study was to investigate the effects of multiple scattering in water clouds, and more specifically, to test some hypotheses about the effects of receiver beam widths on depolarization ratios in stratus clouds. This study represents a step in a progression of studies aimed toward the goal of better understanding the structure of water clouds. The lidar used in this study, a relatively new device, is an instrument which will undoubtedly find increasing applications in atmospheric research. The entire instrument and related data processing equipment fit into the back of a van for easy transport and can be on line and taking data in a single hour.

Cloud droplet induced depolarization from multiple scattering, first thought to jeopardize cloud phase discrimination with lidar, actually contains information on the microphysical characteristics of the cloud. It should be emphasized that by choosing a sufficiently small receiver beam width, the effects on the depolarization ratio of multiple scattering can be minimized. When choosing a small receiver beam width, however, great care must be taken in aligning the system. For receiver beam widths on the order of 1 mrad, a relatively small misalignment in the transmitter/receiver axes can eliminate all single scattering and leave only the multiple scattered component.

In the near future the FIRE (First International Satellite Cloud Climatology Project Regional Experiment) project will investigate marine stratus and stratocumulus, and cirrus clouds to help assess their effects on the earth's energy budget and climate system. Laser systems, used in conjunction with a wide range of other research equipment, are scheduled to be a major component of the FIRE experiments.

During the study described here, lidar measurements have been reported which suggest that stratus cloud microphysical variations may produce characteristic changes in the depolarization ratio. It is recommended that, in order to assess the full information content of polarization lidar observations in stratus clouds, a combined program of lidar measurements, in situ observations of the internal cloud structure, and new multiple scattering theoretical simulations for inhomogeneous clouds be pursued.

REFERENCES

Allen, R.J. and C.M.R. Platt, 1977: Lidar for multiple backscattering and depolarization observations. Appl. Opt., 16, 3193-3199.

Battan, L.J., 1973: Radar Observation of the Atmosphere. The University of Chicago Press, Chicago, 324 pp.

Cai, Q. and K.N. Liou, 1981: Theory of time-dependent multiple backscattering from clouds. J. Atmos. Sci., 38, 1452-1466.

Carswell, A.I. and S.R. Pal, 1980: Polarization anisotropy in lidar multiple scattering from clouds. Appl. Opt., 19, 4123-4126.

Eloranta, E.W., 1972: Calculation of Doubly Scattered Lidar Returns. Ph.D. Dissertation, University of Wisconsin, Madison, 115 pp.

Goodman, J., 1977: The microstructure of California coastal fog and stratus. J. Appl. Meteor., 16, 1056-1067.

Houston, J.D. and A.I. Carswell, 1978: Four-component polarization measurement of lidar atmospheric scattering. Appl. Opt., 17, 614-620.

Liou, K.N. and H. Lahore, 1974: Laser sensing of cloud composition: A backscattered depolarization technique. J. Appl. Meteor., 13, 257-263.

Liou, K.N. and R.M. Schotland, 1971: Multiple backscattering and depolarization from water clouds for a pulsed lidar system. J. Atmos. Sci., 28, 772-784.

Noonkester, V.R., 1984: Droplet spectra observed in marine stratus cloud layers. J. Atmos. Sci., 41, 829-845.

Pal, S.R. and A.I. Carswell, 1973: Polarization properties of lidar backscattering from clouds. Appl. Opt., 12, 1530-1535.

Pal, S.R. and A.I. Carswell, 1976: Multiple scattering in atmospheric clouds: Lidar observations. Appl. Opt., 15, 1990-1995.

Pruppacher, H.R. and J.D. Klett, 1980: Microphysics of Clouds and Precipitation. D. Reidel, Boston, 714 pp.

Randall, D.A., J.A. Coakley, Jr., C.W. Fairall, R.A. Kropfli and D.H. Lenschow, 1984: Outlook for research on subtropical marine stratiform clouds. Bull. Amer. Meteor. Soc., 65, 1290-1301.

Ryan, J.S., S.R. Pal and A.I. Carswell, 1979: Laser backscattering from dense water-droplet clouds. J. Opt. Soc. Amer., 69, 60-67.

Ryan, R.T., H.H. Blau, Jr., P.C. von Thuna and M.L. Cohen, 1972: Cloud microstructure as determined by an optical cloud particle spectrometer. J. Appl. Meteor., 11, 149-156.

Sassen, K., 1974: Depolarization of laser light backscattered by artificial clouds. J. Appl. Meteor., 13, 921-933.

Sassen, K., 1976a: Polarization diversity lidar returns from virga and precipitation: Anomalies and the bright band analogy. J. Appl. Meteor., 15, 292-300.

Sassen, K., 1976b: An Evaluation of Polarization Diversity Lidar for Cloud Physics Research. Ph.D. Dissertation, University of Wyoming, Laramie, 389 pp.

Sassen, K., 1977a: Lidar observations of high plains thunderstorm precipitation. J. Atmos. Sci., 34, 1444-1457.

Sassen, K., 1977b: Optical backscattering from near-spherical water, ice, and mixed phase drops. Appl. Opt., 16, 1332-1341.

Sassen, K. and K.N. Liou, 1979: Scattering of polarized lidar light by water droplet, mixed-phase and ice crystal clouds. Part II: Angular depolarizing and multiple-scattering behavior. J. Atmos. Sci., 36, 852-861.

Sassen, K., K.N. Liou, S. Kinne and M. Griffin, 1985: Highly supercooled cirrus cloud water: confirmation and climatic implications. Science, 36, 411-413.

Schotland, R.M., K. Sassen and R. Stone, 1971: Observations by lidar of linear depolarization ratios for hydrometeors. J. Appl. Meteor., 10, 1011-1017.

Shipley, S.T., E.W. Eloranta and J.A. Weinman, 1974: Measurement of rainfall rates by lidar. J. Appl. Meteor., 13, 800-807.

Spinhirne, J.D., M.Z. Hansen and J. Simpson, 1983: The structure and phase of cloud tops as observed by polarization lidar. J. Clim. Appl. Meteor., 22, 1319-1331.

VITA

Name	Richard Lee Petrilla
Birthdate	March 21, 1948
Birthplace	Cleveland, Ohio
High School	Benedictine High School Cleveland, Ohio
Universities	Cleveland State University Cleveland, Ohio 1966-1967
	University of Tampa Tampa, Florida 1971-1972
	University of Albuquerque Albuquerque, New Mexico 1973-1974
	Texas A & M University College Station, Texas 1978-1980
	University of Utah Salt Lake City, Utah 1983-1985
Degrees	B.S., 1980 Meteorology Texas A & M University College Station, Texas
Professional Society	American Meteorological Society

END

FILMED

12-85

DTIC